
SAFE-SVD: Sensitivity-Aware Fidelity-Enforcing SVD for Physics Foundation Models

Chengjie Hong², Feixiang He³, Yiheng Zeng², Lulu Kang⁴, He Wang^{1,2*}

¹AI Centre, University College London, UK ²University College London, UK
³Central South University, China ⁴ University of Massachusetts at Amherst, US

Abstract

We propose a new method for compressing physics foundation models (PFMs) which is a new trend in AI for Science. While model compression is essential for reducing memory use and accelerating inference in large foundation models, it remains under-explored for PFMs, where preserving physical fidelity is crucial. The challenge lies in the functional nature of physics data, where partial derivatives encode spatiotemporal dynamics and exhibit high sensitivity to compression. Conventional compression methods ignore this structure, often causing severe performance degradation or failure. To address this, we introduce a sensitivity-aware fidelity-enforcing compression framework that explicitly models loss-aware layer sensitivity in the output function space during compression. This provides a new route to compressing scientific foundation models while preserving accuracy and physical fidelity. Experiments show substantial gains over existing methods across multiple models and datasets, achieving significantly higher compression ratios while maintaining accuracy, in some cases by orders of magnitude. More broadly, the work potentially leads to a new subfield of efficient, deployable, and sustainable scientific foundation models in AI for Science.

1 Introduction

Physics foundation models (PFMs), analogous to foundational models in natural language processing, have emerged as general-purpose pre-trained models for a broad range of downstream scientific tasks, from simulation acceleration [3, 19] to weather forecasting [12, 18]. Their success has sparked growing research interest [22, 8, 21]. However, as PFMs continue to scale, their increasing computational demands make fine-tuning and inference prohibitively expensive, limiting practical deployment. In parallel, model compression has proven effective for reducing the computational costs of large neural networks while preserving task performance [29]. Yet despite rapid advances in compression for general foundation models, compression for PFMs remains largely unexplored.

Compressing PFMs presents unique challenges beyond those encountered in conventional foundation models. Unlike models trained on discrete data (*e.g.* images or text), PFMs learn mappings over continuous function spaces defined over space and time, aiming not only to predict system behavior but also to capture governing dynamics and underlying physical laws. Consequently, compression must preserve not only predictive accuracy but also *physical fidelity*, including conservation laws, structural invariants, and higher-order derivative behavior. For example, in incompressible fluid modeling, accurate velocity prediction alone is insufficient if mass conservation is violated. Compression methods that neglect such constraints can produce physically implausible predictions or unstable long-term simulations.

In this work, we focus on low-rank compression based on Singular Value Decomposition (SVD), a widely adopted technique due to its mathematical simplicity, hardware efficiency, and structured

*Corresponding author, he_wang@ucl.ac.uk

parameter reduction. While SVD-based compression has been extensively studied for large language models [1] and more recently multimodal architectures [15, 11], existing approaches are poorly suited to PFMs. A central limitation is that they optimize compression primarily around parameter reconstruction or task accuracy, without accounting for how layer-wise compression perturbations affect physical fidelity in the output function space. In particular, we observe that network layers contribute unequally to preserving physical structure, while their effects are strongly coupled through cross-layer error propagation. Existing methods either treat layer importance independently [9], compress layers separately [26, 27], or only partially model propagated compression errors without differentiating physics-sensitive layers [10]. Moreover, these coupled dependencies make rank allocation especially challenging: manual tuning does not scale to large PFMs, while joint cross-layer optimization is highly non-convex [25]. As a result, existing methods may preserve strong zeroth-order numerical accuracy while violating fundamental physical laws.

To address these challenges, we propose a physics-aware SVD compression framework tailored for PFMs. Our key idea is to align compression with physical fidelity by analyzing the output function in Sobolev space, explicitly modeling sensitivity across multiple orders of partial derivatives with respect to network layers. Building on this, we perform sequential layer-wise compression while jointly accounting for intra-layer reconstruction quality and cross-layer error propagation. Guided by these sensitivity and dependency signals, we further introduce a greedy rank allocation strategy that adaptively computes desired compression ratio on different layers. We evaluate our method on multiple PFMs, including Poseidon [8], VICON [4], and MPP [17], across diverse datasets and physical systems, demonstrating consistent improvements in compression ratio, predictive performance, and physical fidelity. Our contributions are summarized as follows:

- We propose, to the best of our knowledge, the first SVD-based physics-aware model compression framework for PFMs.
- We introduce a novel SVD-based method that jointly accounts for intra-layer reconstruction error, cross-layer perturbation propagation, and physics-informed layer importance.
- We develop a practical rank allocation strategy for scalable physics-aware compression.
- We conduct extensive experiments demonstrating significantly improved compression ratios, predictive accuracy, and physical fidelity across multiple PFMs and scientific domains.

2 Related Work

Existing methods can be divided into pruning, quantization, knowledge distillation, and low-rank approximation. Pruning removes redundant parameters, but either requires specialized hardware for acceleration or can incur substantial accuracy loss [7, 2, 16, 28]. Quantization achieves strong memory savings, but depends on hardware support and optimized kernels, and aggressive low-bit settings often degrade accuracy [5, 14, 20]. Knowledge distillation transfers knowledge from a large teacher model to a smaller student model, but typically requires costly retraining, which is expensive for billion-scale models [32, 24]. Comparatively, low-rank approximation is an attractive hardware-agnostic post-training alternative.

SVD is a widely used low-rank approximation method for model compression. Some methods mainly focus on local reconstruction to minimize layer-wise output error, relying on *e.g.* activation whitening [26], and input shift and error propagation modeling [10]. However, these methods are local methods and are not directly linked to the global objective, *e.g.* in our case task-specific or physics-fidelity losses. To this end, weight importance can be estimated w.r.t. the global objective [9], but with high computational costs while still ignoring cross-layer dependencies. Also, all the above methods are based on uniform rank selection. In contrast, other methods focus on non-uniform rank allocation to layers. They are based on heuristics [30, 27] or joint rank optimization [25], but both are suboptimal for highly sensitive layers. Some methods consider layer sensitivity during rank allocation [6], but without linking layer sensitivity to the global objective, hence also a local method.

3 Methodology

Our method is built on three key insights. First, to balance optimization tractability and compression quality, we adopt a sequential layer-wise compression scheme, where the compression of each layer is conditioned on the previously compressed layers while explicitly modeling the propagation

of compression-induced errors across layers. Second, since layers contribute differently to the physical fidelity of the output, we introduce a physics-aware sensitivity metric which quantifies layer importance through its impact on the final loss, consisting of the original model loss augmented by an additional loss term defined in the Sobolev space. Unlike existing work [9] which operates directly on model weights, inevitably leading to high computational cost for large models and insufficient modeling of layer sensitivity, our method operates on intermediate activations, enabling more efficient compression and effective sensitivity modeling. Third, under a global compression target, we propose a greedy rank allocation strategy which adaptively controls compression intensity across layers according to their estimated contribution to model performance.

3.1 Problem Formulation

Consider a pretrained model of N linear layers with weights $\{\mathbf{W}_i\}_{i=1}^N$. Let $\{\mathbf{X}_i\}_{i=1}^N$ denote the corresponding intermediate activations, where \mathbf{X}_1 is the model input. \mathbf{X}_i are random variables sampled from the data. After compression, the corresponding weights and activations become $\{\mathbf{W}'_i\}_{i=1}^N$ and $\{\mathbf{X}'_i\}_{i=1}^N$, respectively. Since joint optimization across all layers is difficult, we adopt a sequential layer-wise compression scheme which starts from the first layer and processes one layer at a time while propagating the effects of previously compressed layers. For a given layer, let the full-precision output be $\mathbf{Z} = \mathbf{W}\mathbf{X}$ omitting the subscripts for brevity. In deep networks, the input activation \mathbf{X} itself is already perturbed by previous compression, so the actual compressed output becomes $\mathbf{Z}' = \mathbf{W}'\mathbf{X}'$. We represent the resulting perturbation as $\Delta\mathbf{Z} = \mathbf{Z}' - \mathbf{Z}$.

Loss-Aware Objective. To preserve both predictive accuracy and physical fidelity, existing methods based on local reconstruction are insufficient [30, 26, 10]. Therefore, we consider the effect of the intermediate perturbation $\Delta\mathbf{Z}$ on the final loss \mathcal{L} , which consists of the original model loss and a new loss in the Sobolev space (See Appendix C.3). In [13], the loss change $\Delta\mathcal{L} = \mathcal{L}(\mathbf{W} + \Delta\mathbf{W}) - \mathcal{L}(\mathbf{W})$ is approximated by a Taylor series up to the second-order term. Then minimizing the expectation of $\Delta\mathcal{L}$ can be approximated by:

$$\min_{\Delta\mathbf{W}} \mathbb{E}[\Delta\mathcal{L}] \approx \min_{\Delta\mathbf{Z}} \frac{1}{2} \mathbb{E}[\Delta\mathbf{Z}^\top \mathbf{F}_z \Delta\mathbf{Z}], \quad (1)$$

where $\mathbf{F}_z = \mathbf{g}\mathbf{g}^\top$ and $\mathbf{g} = \nabla_{\mathbf{z}}\mathcal{L}$. However, for PFMs, this would mean maintaining a per-sample \mathbf{F}_z for all data samples, which is prohibitively expensive in both memory and computation. Therefore, we approximate \mathbf{F}_z by its expectation $\mathbf{F}_z = \mathbb{E}[\mathbf{g}\mathbf{g}^\top]$ over the whole calibration distribution, *i.e.* the Fisher Information Matrix (FIM) A.1. We refer to the sensitivity based on this approximation as Fisher-based sensitivity. In practice, \mathbf{F}_z is symmetric positive definite E.3, then:

$$\min_{\Delta\mathbf{Z}} \frac{1}{2} \mathbb{E}[\Delta\mathbf{Z}^\top \mathbf{F}_z \Delta\mathbf{Z}] = \min_{\Delta\mathbf{Z}} \frac{1}{2} \mathbb{E}[\|\mathbf{L}\Delta\mathbf{Z}\|_2^2], \quad (2)$$

where $\mathbf{F}_z = \mathbf{L}^\top \mathbf{L}$ is its Cholesky decomposition. Then $\mathbf{L}\Delta\mathbf{Z}$ provides a principled measure of layer sensitivity with respect to the loss, and prioritizes perturbations that are most critical to preserving the physical fidelity included in the loss.

Substituting $\Delta\mathbf{Z}$ into Equation 2, we obtain the layer-wise compression objective:

$$\min_{\mathbf{W}'} \frac{1}{2} \mathbb{E}[\|\mathbf{L}(\mathbf{W}\mathbf{X} - \mathbf{W}'\mathbf{X}')\|_2^2]. \quad (3)$$

However, we observe that optimizing this objective can be unstable and prone to overfitting to the calibration data. Empirically, we find that adding a regularization can improve stability and generalization. The regularization is an intra-layer reconstruction regularizer based on the clean input \mathbf{X} , which captures the reconstruction error of current compressing a layer, *i.e.* $\mathbf{W}\mathbf{X} - \mathbf{W}'\mathbf{X}$. We further introduce a coefficient $\alpha \in (0, 1)$ to balance the intra-layer reconstruction error and the propagated error:

$$\min_{\mathbf{W}'} (1 - \alpha) \underbrace{\mathbb{E}[\|\mathbf{L}(\mathbf{W}\mathbf{X} - \mathbf{W}'\mathbf{X})\|_2^2]}_{\text{intra-layer reconstruction error}} + \alpha \underbrace{\mathbb{E}[\|\mathbf{L}(\mathbf{W}\mathbf{X} - \mathbf{W}'\mathbf{X}')\|_2^2]}_{\text{propagated error}}. \quad (4)$$

A similar strategy of combining the intra-layer reconstruction error and the propagated error has also been recently employed in [10]. However, the key difference is, while both of their errors are purely local to a layer, ours is global and measures loss-aware layer sensitivity by introducing \mathbf{L} .

Calibration. We assume access to a small calibration set $\mathcal{D}_{\text{cal}} = \{(x_i, y_i)\}_{i=1}^{N_{\text{cal}}}$ from the training data, where (x_i, y_i) is an input-output pair. These samples are only used to estimate activation statistics and compute the FIM to minimize Equation 4 from the original model.

3.2 Optimization via Low-Rank Approximation

Although directly minimizing Equation 4 subject to a pre-defined rank is possible, prior studies [30, 26] show that using SVD is an efficient solution, which requires to minimize the trace-equivalent form Equation 4 using the identity $\|\mathbf{a}\|_2^2 = \text{Tr}(\mathbf{a}\mathbf{a}^\top)$ (see Appendix A.2):

$$\min_{\mathbf{W}'} -2 \text{Tr}(\mathbf{L}\mathbf{W}'\boldsymbol{\Sigma}_{\text{cov}}\mathbf{W}'^\top\mathbf{L}^\top) + \text{Tr}(\mathbf{L}\mathbf{W}'\boldsymbol{\Sigma}_{\text{c_cov}}\mathbf{W}'^\top\mathbf{L}^\top) + \text{const}, \quad (5)$$

where

$$\boldsymbol{\Sigma}_{\text{cov}} = (1 - \alpha)\boldsymbol{\Sigma}_{\mathbf{X}\mathbf{X}} + \alpha\boldsymbol{\Sigma}_{\mathbf{X}'\mathbf{X}}, \quad \boldsymbol{\Sigma}_{\text{c_cov}} = (1 - \alpha)\boldsymbol{\Sigma}_{\mathbf{X}\mathbf{X}} + \alpha\boldsymbol{\Sigma}_{\mathbf{X}'\mathbf{X}'} \quad (6)$$

In practice, $\boldsymbol{\Sigma}_{\text{c_cov}}$ is positive definite (see Appendix E.3), allowing a Cholesky decomposition $\boldsymbol{\Sigma}_{\text{c_cov}} = \mathbf{R}\mathbf{R}^\top$. Substituting this factorization into Equation 5, this problem can be rewritten as a Frobenius-norm regression task (see Appendix A.3):

$$\min_{\mathbf{W}'} \|\mathbf{L}\mathbf{W}'\mathbf{R} - \mathbf{L}\mathbf{W}\boldsymbol{\Sigma}_{\text{cov}}^\top\mathbf{R}^{-\top}\|_F^2, \quad (7)$$

where if we define $\mathbf{M} = \mathbf{L}\mathbf{W}'\mathbf{R}$ and $\mathbf{M}^* = \mathbf{L}\mathbf{W}\boldsymbol{\Sigma}_{\text{cov}}^\top\mathbf{R}^{-\top}$, then the optimization problem reduces to a standard low-rank approximation:

$$\min_{\mathbf{M}} \|\mathbf{M} - \mathbf{M}^*\|_F^2 \quad \text{subject to } \text{rank}(\mathbf{M}) = k. \quad (8)$$

By the Eckart–Young–Mirsky theorem, the optimal rank- k solution is obtained by truncating \mathbf{M}^* and mapping it back to the original parameter space and obtaining the compressed weight matrix:

$$\mathbf{M} = \text{SVD}_k(\mathbf{M}^*), \quad \mathbf{W}' = \mathbf{L}^{-1}\mathbf{M}\mathbf{R}^{-1}. \quad (9)$$

3.3 Loss-aware Rank Allocation

Optimizing Equation 8 essentially comes down to choosing k for each layer, which is a combinatorial optimization problem [31]. In practice, existing research often resorts to heuristics which are compatible with their specific optimization formulations [30, 27, 25]. Similarly, we propose a greedy algorithm to allocate ranks to each layer, subject to a pre-defined compression ratio.

In the sequential compression setting, directly optimizing the rank of \mathbf{M}^* is intractable because $\mathbf{M}^* = \mathbf{L}\mathbf{W}\boldsymbol{\Sigma}_{\text{cov}}^\top\mathbf{R}^{-\top}$ depends on perturbed activations \mathbf{X}' , which are unavailable before compression. To circumvent this, we factorize the clean covariance $\boldsymbol{\Sigma}_{\mathbf{X}\mathbf{X}} = \mathbf{R}^c\mathbf{R}^{c\top}$ and observe that when the perturbation is small, *i.e.* $\mathbf{X}' \approx \mathbf{X}$, we have $\mathbf{M}^* \approx \mathbf{L}\mathbf{W}\mathbf{R}^c$, so the singular values of $\mathbf{L}\mathbf{W}\mathbf{R}^c$ serve as a reliable proxy for rank selection. Even under high compression ratios where the perturbation is no longer negligible, we empirically find that it remains an effective proxy for rank selection.

Greedy Global Rank Allocation. Building on the SVD described above, we formulate the rank selection task as a global resource allocation problem across all N linear layers. For each layer l with its weight matrix $\mathbf{W}_l \in \mathbb{R}^{d_{\text{out}}^{(l)} \times d_{\text{in}}^{(l)}}$, its rank- k_l approximation is factorized as

$$\mathbf{W}_l \approx \mathbf{W}_{l,k_l} = (\mathbf{U}_l\boldsymbol{\Sigma}_{l,k_l}^{1/2})(\boldsymbol{\Sigma}_{l,k_l}^{1/2}\mathbf{V}_l^\top). \quad (10)$$

Increasing the rank by one corresponds to adding one singular component to \mathbf{W}_{l,k_l} , *i.e.* one column to $\mathbf{U}_l\boldsymbol{\Sigma}_{l,k_l}^{1/2}$ and one row to $\boldsymbol{\Sigma}_{l,k_l}^{1/2}\mathbf{V}_l^\top$. The resulting cost is therefore $P^{(l)} = d_{\text{out}}^{(l)} + d_{\text{in}}^{(l)}$. To satisfy a target compression ratio $\eta \in (0, 1]$, we impose the global budget

$$B = \eta \cdot \sum_{l=1}^N (d_{\text{out}}^{(l)} \times d_{\text{in}}^{(l)}), \quad (11)$$

where $d_{\text{out}}^{(l)} \times d_{\text{in}}^{(l)}$ is the number of parameters in linear layer l and $\sum_{l=1}^N (d_{\text{out}}^{(l)} \times d_{\text{in}}^{(l)})$ is the total number of parameters of the uncompressed model. So B is the total number of parameters that need

to be retained. Under this budget, our rank allocation method decides which singular components should be retained across all layers.

For each layer, we evaluate every candidate singular component from the matrix $\mathbf{L}_l \mathbf{W}_l \mathbf{R}_l^c$, whose i -th singular value is denoted as $\sigma_{l,i}$. Under the second-order Taylor approximation, retaining this component yields an estimated reduction in loss degradation proportional to $\sigma_{l,i}^2$, see Appendix A.4. Since a retained component at layer l incurs the cost $P^{(l)}$, we define its benefit-cost ratio as $v_{l,i} = \sigma_{l,i}^2 / P^{(l)}$. We then rank all candidate components from all layers by $v_{l,i}$ and greedily retain them in descending order until no remaining candidate can be selected without exceeding the budget.

The overall allocation is detailed in Algorithm 1: (i) **SVD**. Compute the singular values $\{\sigma_{l,i}^2\}$ of $\mathbf{L}_l \mathbf{W}_l \mathbf{R}_l^c$. (ii) **Scoring**. Evaluate the score $v_{l,i}$ for all candidate rank-1 components in all layers. (iii) **Ranking**. Merge all candidates and sort them by $v_{l,i}$ in descending order. (iv) **Selection**. Iteratively select the highest-scoring component, increase the corresponding k_l by one, and subtract P_l from the remaining budget until the budget is exhausted. This yields the global rank configuration $\{k_1, \dots, k_N\}$, which is then used to compute the optimal compressed weight matrix \mathbf{W}'_l according to Equation 9.

Algorithm 1 Greedy Global Rank Allocation

Require: Budget B , Layer matrices $\{L_l W_l R_l^c\}_{l=1}^N$, Unit costs $\{P^{(l)}\}_{l=1}^N$
Ensure: Rank configuration $\{k_l\}_{l=1}^N$

- 1: Initialize $k_l \leftarrow 0$ for all $l \in \{1, \dots, N\}$, and $\text{cost} \leftarrow 0$
- 2: $\mathcal{C} \leftarrow \bigcup_{l=1}^N \left\{ \left(\frac{\sigma_{l,i}^2}{P_l}, l \right) \mid \sigma_{l,i} \in \text{SVD}(L_l W_l R_l^c) \right\}$ {Global efficiency pool}
- 3: Sort \mathcal{C} in descending order by efficiency score $v = \sigma^2 / P$
- 4: **for** each $(v, l) \in \mathcal{C}$ **do**
- 5: **if** $\text{cost} + P^{(l)} \leq B$ **then**
- 6: $k_l \leftarrow k_l + 1$
- 7: $\text{cost} \leftarrow \text{cost} + P^{(l)}$
- 8: **else**
- 9: **continue** {Skip this component because it would exceed the budget}
- 10: **end if**
- 11: **end for**
- 12: **return** $\{k_1, k_2, \dots, k_N\}$

4 Experiments

We evaluate our method on three representative PFMs: Poseidon [8] VICON [4] and MPP [17]. We only show partial results on Poseidon and VICON in the main paper due to space limit and give additional results in Appendix B. For Poseidon, we fine-tune the pretrained model on three PDE families: incompressible Navier–Stokes, compressible Euler, and acoustic wave equations. We report one representative benchmark from each family, namely NS-PwC, CE-RM, and Wave-Gaussian. In contrast, VICON is a unified model designed for multiple domains, and is evaluated separately on each domain. Calibration data are sampled from the corresponding training sets. For Poseidon, we construct the calibration set from 64 trajectories, using 210 samples per trajectory for Navier–Stokes and compressible Euler tasks, and 120 samples per trajectory for wave tasks. For VICON, we construct a fused calibration dataset from its supported domains [23]. Specifically, we use 2,048 calibration samples per scenario for VICON. All experiments are conducted on NVIDIA H200 GPUs. More details are presented in the Appendix C.

Baselines We compare our method with five representative SVD-based compression baselines which cover the major design dimensions of low-rank model compression, such as rank selection and weight reconstruction techniques. To ensure a fair comparison and focus on the effectiveness of compression, all methods are evaluated post-training without any additional fine-tuning. **FWSVD** [9] performs Fisher-based layer-wise compression. **ASVD** [30] applies activation-aware scaling before SVD decomposition. **SVD-LLM V2** [27] improves layer-wise calibration and reconstruction for large models. **Dobi-SVD** [25] performs joint cross-layer rank optimization over all layers simultaneously.

Table 1: Ablation study on NS-BB. RS: rank selection; SE: sensitivity estimation; SL Type: Sobolev loss type; SL order: Sobolev order; α : trade-off coefficient.

Components					Size	Base Loss↓	Sobolev↓	Div-free↓	Vorticity↓
RS	SE	SL Type	SL Order	α					
×	×	-	-	-	125.9M	2809%	5018%	2863%	1971%
✓	×	-	-	-	126.3M	63.92%	361.9%	126.1%	60.23%
✓	✓	l_2	0	0.5	126.3M	36.69%	168.8%	49.50%	19.97%
✓	✓	l_2	1	0.5	126.3M	37.52%	162.6%	45.53%	18.50%
✓	✓	l_2	2	0.5	126.3M	34.35%	152.2%	41.89%	17.33%
✓	✓	l_1	0	0.5	126.3M	19.72%	95.76%	23.84%	11.84%
✓	✓	l_1	1	0.5	126.3M	2.85%	7.23%	1.15%	1.17%
✓	✓	l_1	2	0.5	126.3M	1.22%	0.66%	0.26%	0.74%
✓	✓	l_1	2	0.3	126.3M	1.32%	0.59%	0.24%	0.75%
✓	✓	l_1	2	0.7	126.3M	1.20%	0.83%	0.29%	0.77%

SAES-SVD [10] further accounts for both intra-layer reconstruction error and inter-layer propagation error. Together, these methods span Fisher-based, activation-aware, globally optimized, and error-propagated compression strategies, providing strong baselines for comparison.

Metrics. We evaluate compression performance using two categories of metrics. General metrics measure overall predictive accuracy and functional smoothness, including the model’s original loss (*e.g.* relative l_1 or MSE, depending on the backbone) and the Sobolev loss (physically meaningful derivatives depending on the PDE class, *e.g.* second-order for Navier–Stokes equations), which captures consistency in both field values and derivative structures between the original model and compressed model. We additionally report PDE-specific metrics that capture task-dependent physical constraints. For incompressible Navier–Stokes, we evaluate divergence-free error and vorticity accuracy to assess incompressibility and rotational dynamics. To ensure fair comparison across models, datasets, and metrics with different numerical scales, all results are reported as absolute percentage changes relative to the uncompressed model (Origin). Detailed definitions of all metrics are provided in the Appendix C.3.

4.1 Ablation Study

We separately evaluate our layer dependency modeling, layer sensitivity estimation (SE), and rank selection (RS). To test layer dependency, we use a base model without the Sobolev loss, loss-aware layer sensitivity, and rank selection. Then we add rank selection. Next, for SE, we add the Sobolev loss and loss-aware layer sensitivity. The Sobolev term includes derivatives of orders 0/1/2 to capture the principal physical structures, and is evaluated using both l_2 and l_1 norms. We evaluate different variants on Poseidon fine-tuned on NS-BB, with results reported in Table 1.

Our base model implemented as $\mathbb{E}[\|\mathbf{W}\mathbf{X} - \mathbf{W}'\mathbf{X}\|_2^2 + \|\mathbf{W}\mathbf{X} - \mathbf{W}'\mathbf{X}'\|_2^2]$ with uniform rank allocation, ignores both cross-layer dependencies and the impact of compression on the final output, resulting in severe degradation, with errors increasing by nearly 2000% on several metrics. Replacing uniform allocation with the proposed RS substantially improves performance: reducing relative increase to 63.91% for Base Loss, 361.9% for Sobolev Loss, 126.1% for Divergence, and 60.23% for Vorticity, demonstrating the effectiveness of our global rank selection. Incorporating SE further improves performance. While the formulation is naturally aligned with l_2 norm, we empirically find that the l_1 variant yields better results and adopt it in our implementation. Under Order-0 with SE and l_1 , the error are reduced to 19.70%, 95.76%, 23.84%, and 11.84%, respectively. Increasing the order consistently improves performance: Order-1 reduces errors to 2.84%, 7.23%, 1.15%, and 1.17%, while Order-2 achieves the best overall results with only 1.22%, 0.66%, 0.26%, and 0.74% degradation. These trends indicate that higher-order Sobolev losses lead to more accurate layer sensitivity estimation and better preservation of physical structures of derivatives. Varying α further demonstrates the importance of layer dependency modeling. The balanced setting $\alpha = 0.7$ achieves the lowest Base Loss while remaining competitive on physics-related metrics. This suggests that jointly balancing local reconstruction and cross-layer propagation is critical. Overall, the ablation confirms that loss-aware layer sensitivity, cross-layer error propagation, and global rank selection are all necessary for high-fidelity compression of PFMs.

Table 2: Experimental Results on Poseidon

Poseidon	Size	NS-PwC				CE-RM		Wave-Gauss		
		Base Loss ↓	Sobolev ↓	Div-Free ↓	Vorticity ↓	Base Loss ↓	Sobolev ↓	Base Loss ↓	Sobolev ↓	
1	Origin	628.6M	0.00%	0.00%	0.00%	0.00%	0.00%	0.00%	0.00%	
0.6	ASVD	376.9M	4496%	2680%	2017%	2805%	25.39%	6.61%	352.1%	6202%
	FWSVD	377.1M	7124%	2977%	1700%	3727%	23.24%	8.51%	569.7%	2415%
	SVD-LLM V2	438.3M	7038%	2449%	1482%	3651%	26.78%	9.31%	576.4%	4982%
	Dobi-SVD	378.1M	7468%	3036%	2137%	3719%	35.70%	24.58%	658.6%	9210%
	SAES-SVD	377.1M	2882%	1763%	1572%	1863%	2.19%	2.53%	225.8%	3354%
	Ours	377.5M	0.00%	0.01%	0.00%	0.01%	0.00%	0.00%	0.00%	0.01%
0.4	ASVD	251.4M	5169%	4364%	2773%	3311%	34.10%	15.79%	475.4%	14572%
	FWSVD	251.5M	7846%	5080%	2449%	3961%	28.33%	28.64%	588.1%	3542%
	SVD-LLM V2	374.9M	8741%	6051%	4530%	4131%	35.87%	54.99%	656.0%	19627%
	Dobi-SVD	252.6M	8481%	5206%	2709%	4048%	39.27%	25.91%	670.4%	10497%
	SAES-SVD	251.5M	3062%	1868%	1632%	1967%	3.46%	6.18%	249.3%	4020%
	Ours	251.9M	0.26%	0.08%	0.03%	0.17%	0.01%	0.05%	0.04%	0.40%
0.2	ASVD	125.8M	6725%	6183%	3563%	4167%	41.02%	80.05%	525.0%	13007%
	FWSVD	125.9M	8622%	7650%	3770%	4276%	40.57%	97.34%	655.1%	11452%
	SVD-LLM V2	353.2M	9529%	6011%	4183%	4434%	61.44%	66.29%	1122%	19865%
	Dobi-SVD	127.0M	8774%	10090%	4999%	4440%	44.78%	29.72%	728.6%	20124%
	SAES-SVD	125.9M	3726%	2429%	2199%	2426%	6.25%	9.83%	366.9%	5873%
	Ours	126.3M	2.64%	1.79%	0.52%	1.35%	0.10%	1.01%	0.70%	151.9%

Table 3: Experimental Results on VICON

VICON	Size	NS-2D				Comp-2D		Euler-2D		
		Base Loss ↓	Sobolev ↓	Div-Free ↓	Vorticity ↓	Base Loss ↓	Sobolev ↓	Base Loss ↓	Sobolev ↓	
1	Origin	87.8M	0.00%	0.00%	0.00%	0.00%	0.00%	0.00%	0.00%	
0.6	ASVD	52.4M	10140%	528.7%	7.01%	476.1%	41318%	1394%	2692%	97.36%
	FWSVD	52.7M	1861%	302.3%	2.23%	357.5%	7885%	947.6%	805.1%	57.72%
	SVD-LLM V2	52.7M	73.76%	11.74%	5.30%	43.87%	260.0%	60.00%	47.26%	3.31%
	Dobi-SVD	52.9M	1968%	109.3%	24.08%	163.6%	757.4%	260.1%	128.6%	18.49%
	SAES-SVD	52.7M	49.63%	7.06%	3.92%	26.01%	144.7%	33.70%	36.66%	25.99%
	Ours	52.8M	2.07%	1.22%	0.21%	3.08%	16.54%	3.82%	3.08%	28.35%
0.4	ASVD	33.5M	13064%	532.5%	11.34%	490.4%	46290%	1382%	2865%	94.70%
	FWSVD	35.2M	4862%	349.7%	3.24%	437.5%	22440%	1155%	2010%	69.01%
	SVD-LLM V2	35.7M	689.5%	32.06%	10.96%	136.1%	2152%	163.9%	265.6%	16.69%
	Dobi-SVD	37.0M	2607%	113.3%	34.70%	209.6%	1795%	285.9%	278.3%	13.58%
	SAES-SVD	35.2M	156.3%	18.10%	8.68%	68.40%	609.3%	74.10%	115.5%	20.65%
	Ours	35.3M	24.98%	4.23%	0.85%	11.32%	127.4%	26.40%	27.05%	26.91%
0.2	ASVD	16.5M	15583%	535.6%	12.51%	484.5%	48919%	1392%	3016%	94.46%
	FWSVD	17.7M	11265%	295.8%	29.67%	462.3%	43908%	1232%	2769%	66.10%
	SVD-LLM V2	18.3M	2245%	67.19%	40.38%	290.2%	16822%	399.9%	1230%	34.89%
	Dobi-SVD	20.2M	3705%	118.8%	46.52%	262.2%	4929%	358.1%	630.2%	7.02%
	SAES-SVD	17.7M	651.3%	37.96%	16.22%	165.2%	2952%	169.7%	432.3%	12.12%
	Ours	17.8M	291.1%	23.19%	7.87%	76.27%	1051%	99.28%	291.8%	16.10%
Ours*	17.8M	239.7%	20.17%	8.07%	66.31%	927.2%	116.8%	248.3%	17.75%	

4.2 Comparisons on Poseidon

We consider three representative scenarios: NS-PwC, CE-RM, and Wave-Gaussian, with results reported in Table 2. These tasks cover distinct physical regimes, including sharp-interface incompressible flow, shock-driven turbulent mixing, and smooth wave propagation.

Across all three scenarios, our method consistently outperforms all baselines across every compression ratio. Under 60% compression (ratio 0.6), the compressed models remain nearly indistinguishable from the original models across all three tasks. Even at 40% compression (ratio 0.4), the degradation of our method stays below 0.5% on nearly all reported metrics, demonstrating strong robustness under aggressive compression. At the most extreme setting (20% remaining parameters, ratio 0.2), performance remains strong on NS-PwC and CE-RM, while Wave-Gaussian shows larger increases in Sobolev Loss, although still substantially outperforming all baselines. This trend is consistent with the underlying physics. NS-PwC and CE-RM are primarily governed by localized structures such as vortices, transport fronts, and shocks, where errors tend to remain spatially concentrated. By contrast, Wave-Gaussian is dominated by globally coherent propagating modes, making it more sensitive to small compression-induced perturbations that accumulate as phase shifts and wave-speed errors.

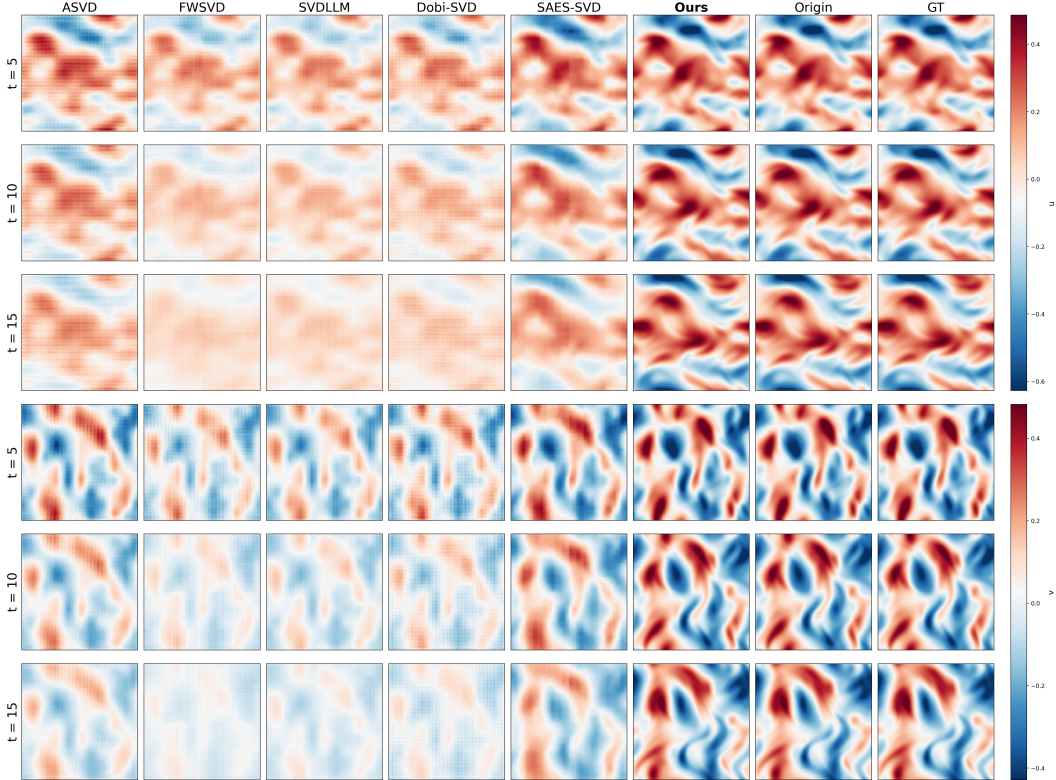


Figure 1: Predicted velocity fields (u, v) on the NS-PwC dataset at compression ratio 0.2 over three rollout horizons ($t = 5, 10, 15$).

4.3 Comparisons on VICON

Unlike Poseidon, which is fine-tuned separately on each dataset prior to compression, VICON is a unified model trained across multiple physical domains. To account for this multi-domain setting, we evaluate two variants of our method: Ours and Ours*. Both use fused multi-scenario calibration, while Ours* further reweights dataset contributions using energy balance to mitigate cross-domain scale disparities during compression. Further details are provided in the Appendix D.

Evaluation results are summarized in Table 3. Overall, our method consistently achieves the best or near-best trade-off across datasets and compression levels. Under aggressive compression (ratio 0.2), all methods suffer a sharp increase in Base Loss, indicating that the remaining model capacity is insufficient for reliable deployment. Although some baselines achieve lower Sobolev errors in specific cases (e.g., Euler-2D), they come with substantially higher Base Loss, limiting their practical value. In contrast, our method maintains low Base Loss while remaining competitive on Sobolev metrics, resulting in stronger overall solution quality. While Ours outperforms Ours* on certain metrics at specific compression ratios, Ours* delivers better overall performance across settings.

4.4 Qualitative Comparison

NS-PwC Figure 1 compares predicted velocity fields (u, v) on the NS-PwC (Navier–Stokes, Piecewise Constants) dataset. This dataset features turbulent vortex dynamics driven by piecewise-constant initial conditions, producing sharp shear layers and concentrated vortex cores that evolve over time.

Most baselines, FWSVD, SVD-LLM V2, and Dobi-SVD, exhibit severe over-smoothing which progressively erase fine-scale vortical structures; by $t=15$, their predictions become largely featureless, with Dobi-SVD additionally displaying noticeable checkerboard artifacts. ASVD and SAES-SVD preserve more structure than these baselines but still loses sharp gradients and concentrated vortex cores. In contrast, our method remains visually consistent with the original model across all horizons, accurately preserving vortex-pair advection, shear-layer sharpness, and the global energy distribution.

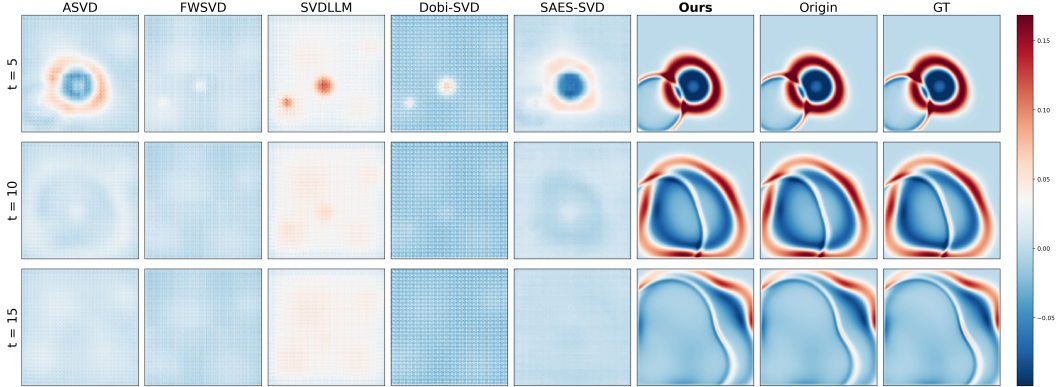


Figure 2: Predicted wave field u on the Wave-Gauss dataset at compression ratio 0.2 over three rollout horizons ($t = 5, 10, 15$).

These observations align with the quantitative results in Table 2: at 0.2 compression ratio, baselines incur Sobolev increases of 2429–10090%, indicating massive gradient degradation, while our method achieves below 3.0% increase in both Base Loss and Sobolev norm.

Wave-Gauss We show one visual comparison in Figure 2 on the Wave-Gauss dataset. This dataset contains wave propagation from Gaussian initial conditions, producing expanding concentric wavefronts that develop complex interference patterns over time. FWSVD, SVD-LLM V2, and Dobi-SVD fail to resolve the expanding circular wavefronts at $t=5$ already and degrade to essentially constant or artifact-dominated outputs by $t=15$. ASVD and SAES-SVD capture the gross wavefront geometry but loses the fine-scale interference patterns. Our method faithfully reproduces both the sharp wavefront edges and the intricate interference structures across all rollout steps, closely tracking the original model. These qualitative results also align with the results in Table 2. At 0.2 compression ratio, baselines exhibit Base Loss increases of 366.9–1122% and Sobolev increases exceeding 10,000%, reflecting a near-total loss of both amplitude and gradient information. Our method maintains a Base Loss increase of only 0.70% and a Sobolev increase of 152%.

5 Conclusion, Limitation, and Future Work

We presented the first physics-aware SVD compression framework, SAFE-SVD, for physics foundation models. As PFMs have started a fundamental shift in AI for Science, SAFE-SVD is timely and proactive to anticipate and address the imminent energy bottleneck caused by ever-growing PFMs. SAFE-SVD considers both predictive accuracy and physical fidelity during compression, which are built in the modeling of layer sensitivity, cross-layer error propagation, and adaptive rank allocation. Experiments on three major PFMs show massive and consistent improvements over existing baselines across diverse PDE tasks and physical metrics.

One limitation is SAFE-SVD is specific to PDE families. This is because we need the loss terms in the Sobolev space where the orders of derivatives are decided by the specific PDE family in the calibration dataset. However, we argue that a calibration dataset is always available in practice as the target application domain is usually given. Moreover, for applications requiring high precision, compression-induced errors may limit the applicability of our method. However, this is a common problem for all compression methods. Also, there are other applications which do not require high precision, *e.g.* inverse design, and can benefit from model compression.

An important direction for future work is to incorporate stronger physics priors, such as conservation laws, symmetries, and geometry-aware constraints. Another promising direction is extending the framework to larger-scale and multimodal scientific foundation models.

References

- [1] Josh Achiam, Steven Adler, Sandhini Agarwal, Lama Ahmad, Ilge Akkaya, Florencia Leoni Aleman, Diogo Almeida, Janko Altenschmidt, Sam Altman, Shyamal Anadkat, et al. Gpt-4

- technical report. *arXiv preprint arXiv:2303.08774*, 2023.
- [2] Saleh Ashkboos, Maximilian L Croci, Marcelo Gennari do Nascimento, Torsten Hoeffler, and James Hensman. Slicept: Compress large language models by deleting rows and columns. *arXiv preprint arXiv:2401.15024*, 2024.
 - [3] Kamyar Azizzadenesheli, Nikola Kovachki, Zongyi Li, Miguel Liu-Schiaffini, Jean Kossaifi, and Anima Anandkumar. Neural operators for accelerating scientific simulations and design. *Nature Reviews Physics*, 6(5):320–328, 2024.
 - [4] Yadi Cao, Yuxuan Liu, Liu Yang, Rose Yu, Hayden Schaeffer, and Stanley Osher. Vicon: Vision in-context operator networks for multi-physics fluid dynamics prediction. *arXiv preprint arXiv:2411.16063*, 2024.
 - [5] Tim Dettmers, Artidoro Pagnoni, Ari Holtzman, and Luke Zettlemoyer. Qlora: Efficient finetuning of quantized llms. *Advances in neural information processing systems*, 36:10088–10115, 2023.
 - [6] Xuan Ding, Rui Sun, Yunjian Zhang, Xiu Yan, Yueqi Zhou, Kaihao Huang, Suzhong Fu, Chuanlong Xie, and Yao Zhu. Dipsvd: Dual-importance protected svd for efficient llm compression. *arXiv preprint arXiv:2506.20353*, 2025.
 - [7] Elias Frantar and Dan Alistarh. Sparsegpt: Massive language models can be accurately pruned in one-shot. In *International conference on machine learning*, pages 10323–10337. PMLR, 2023.
 - [8] Maximilian Herde, Bogdan Raonić, Tobias Rohner, Roger Käppeli, Roberto Molinaro, Emmanuel De Bezenac, and Siddhartha Mishra. Poseidon: Efficient foundation models for pdes. *Advances in Neural Information Processing Systems*, 37:72525–72624, 2024.
 - [9] Yen-Chang Hsu, Ting Hua, Sungen Chang, Qian Lou, Yilin Shen, and Hongxia Jin. Language model compression with weighted low-rank factorization. *arXiv preprint arXiv:2207.00112*, 2022.
 - [10] Xing Hu, Dawei Yang, Yuan Cheng, Zhixuan Chen, and Zukang Xu. Saes-svd: Self-adaptive suppression of accumulated and local errors for svd-based llm compression. *arXiv preprint arXiv:2602.03051*, 2026.
 - [11] Moo Jin Kim, Karl Pertsch, Siddharth Karamcheti, Ted Xiao, Ashwin Balakrishna, Suraj Nair, Rafael Rafailov, Ethan Foster, Grace Lam, Pannag Sanketi, et al. Openvla: An open-source vision-language-action model, 2024. URL <https://arxiv.org/abs/2406.09246>, 1(2):4, 2024.
 - [12] Richard Lam et al. Graphcast: Learning skillful medium-range global weather forecasting. *Science*, 2023.
 - [13] Yuhang Li, Ruihao Gong, Xu Tan, Yang Yang, Peng Hu, Qi Zhang, Fengwei Yu, Wei Wang, and Shi Gu. Brecq: Pushing the limit of post-training quantization by block reconstruction. *arXiv preprint arXiv:2102.05426*, 2021.
 - [14] Ji Lin, Jiaming Tang, Haotian Tang, Shang Yang, Wei-Ming Chen, Wei-Chen Wang, Guangxuan Xiao, Xingyu Dang, Chuang Gan, and Song Han. Awq: Activation-aware weight quantization for on-device llm compression and acceleration. *Proceedings of machine learning and systems*, 6:87–100, 2024.
 - [15] Haotian Liu, Chunyuan Li, Yuheng Li, and Yong Jae Lee. Improved baselines with visual instruction tuning. In *Proceedings of the IEEE/CVF conference on computer vision and pattern recognition*, pages 26296–26306, 2024.
 - [16] Xinyin Ma, Gongfan Fang, and Xinchao Wang. Llm-pruner: On the structural pruning of large language models. *Advances in neural information processing systems*, 36:21702–21720, 2023.
 - [17] Michael McCabe, Bruno Régalo-Saint Blancard, Liam Parker, Ruben Ohana, Miles Cranmer, Alberto Bietti, Michael Eickenberg, Siavash Golkar, Geraud Krawezik, Francois Lanusse, et al. Multiple physics pretraining for spatiotemporal surrogate models. *Advances in Neural Information Processing Systems*, 37:119301–119335, 2024.

- [18] Tung Nguyen, Johannes Brandstetter, Ashish Kapoor, Jayesh K Gupta, and Aditya Grover. Climax: A foundation model for weather and climate. *arXiv preprint arXiv:2301.10343*, 2023.
- [19] Md Ashiqur Rahman, Robert Joseph George, Mogab Elleithy, Daniel Leibovici, Zongyi Li, Boris Bonev, Colin White, Julius Berner, Raymond A Yeh, Jean Kossaifi, et al. Pretraining codomain attention neural operators for solving multiphysics pdes. *Advances in Neural Information Processing Systems*, 37:104035–104064, 2024.
- [20] Yuzhang Shang, Zhihang Yuan, Qiang Wu, and Zhen Dong. Pb-llm: Partially binarized large language models. *arXiv preprint arXiv:2310.00034*, 2023.
- [21] Eduardo Soares, Emilio Vital Brazil, Victor Shirasuna, Breno WSR de Carvalho, and Cristiano Malossi. Towards a foundation model for partial differential equations across physics domains. *arXiv preprint arXiv:2511.21861*, 2025.
- [22] Shashank Subramanian, Peter Harrington, Kurt Keutzer, Wahid Bhimji, Dmitriy Morozov, Michael W Mahoney, and Amir Gholami. Towards foundation models for scientific machine learning: Characterizing scaling and transfer behavior. *Advances in Neural Information Processing Systems*, 36:71242–71262, 2023.
- [23] Makoto Takamoto, Timothy Praditia, Raphael Leiteritz, Daniel MacKinlay, Francesco Alesiani, Dirk Pflüger, and Mathias Niepert. Pdebench: An extensive benchmark for scientific machine learning. *Advances in neural information processing systems*, 35:1596–1611, 2022.
- [24] Lin Wang and Kuk-Jin Yoon. Knowledge distillation and student-teacher learning for visual intelligence: A review and new outlooks. *IEEE transactions on pattern analysis and machine intelligence*, 44(6):3048–3068, 2021.
- [25] Qinsi Wang, Jinghan Ke, Masayoshi Tomizuka, Yiran Chen, Kurt Keutzer, and Chenfeng Xu. Dobi-svd: Differentiable svd for llm compression and some new perspectives. *arXiv preprint arXiv:2502.02723*, 2025.
- [26] Xin Wang, Yu Zheng, Zhongwei Wan, and Mi Zhang. Svd-llm: Truncation-aware singular value decomposition for large language model compression. *arXiv preprint arXiv:2403.07378*, 2024.
- [27] Xin Wang, Samiul Alam, Zhongwei Wan, Hui Shen, and Mi Zhang. Svd-llm v2: Optimizing singular value truncation for large language model compression. In *Proceedings of the 2025 Conference of the Nations of the Americas Chapter of the Association for Computational Linguistics: Human Language Technologies (Volume 1: Long Papers)*, pages 4287–4296, 2025.
- [28] Mengzhou Xia, Tianyu Gao, Zhiyuan Zeng, and Danqi Chen. Sheared llama: Accelerating language model pre-training via structured pruning. *arXiv preprint arXiv:2310.06694*, 2023.
- [29] Canwen Xu and Julian McAuley. A survey on model compression and acceleration for pretrained language models. In *Proceedings of the AAAI Conference on Artificial Intelligence*, volume 37, pages 10566–10575, 2023.
- [30] Zhihang Yuan, Yuzhang Shang, Yue Song, Dawei Yang, Qiang Wu, Yan Yan, and Guangyu Sun. Asvd: Activation-aware singular value decomposition for compressing large language models. *arXiv preprint arXiv:2312.05821*, 2023.
- [31] Xiangyu Zhang, Jianhua Zou, Kaiming He, and Jian Sun. Accelerating very deep convolutional networks for classification and detection. *IEEE transactions on pattern analysis and machine intelligence*, 38(10):1943–1955, 2015.
- [32] Borui Zhao, Quan Cui, Renjie Song, Yiyu Qiu, and Jiajun Liang. Decoupled knowledge distillation. In *Proceedings of the IEEE/CVF Conference on computer vision and pattern recognition*, pages 11953–11962, 2022.

Appendix

A Detailed Derivation of of Physics-Aware Compression

This appendix provides the preliminaries, detailed derivations and rank selection reasoning omitted in the main text. We first introduce the necessary preliminaries, then show how the proposed loss-aware compression objective is derived and demonstrate how the resulting optimization can be reduced to a standard low-rank approximation problem. Finally, we reason why our rank selection is efficient. Throughout, we focus on a single layer and omit the layer index for clarity.

A.1 Preliminaries

Low-Rank Compression via SVD Given a matrix $\mathbf{W} \in \mathbb{R}^{m \times n}$, its Singular Value Decomposition is $\mathbf{W} = \mathbf{U}\mathbf{\Sigma}\mathbf{V}^\top$, where $\mathbf{U} \in \mathbb{R}^{m \times m}$ and $\mathbf{V} \in \mathbb{R}^{n \times n}$ are orthogonal matrices, and $\mathbf{\Sigma} \in \mathbb{R}^{m \times n}$ is diagonal with singular values ordered as $\sigma_1 \geq \sigma_2 \geq \dots \geq \sigma_r > 0$. A rank- k approximation is obtained by truncating the spectrum $\mathbf{W} \approx \mathbf{W}_k = \mathbf{U}\mathbf{\Sigma}_k\mathbf{V}^\top$ where $\mathbf{\Sigma}_k$ contains only the top k singular values. By the Eckart–Young–Mirsky theorem, \mathbf{W}_k is the optimal rank- k approximation under the Frobenius norm. Furthermore, \mathbf{W}_k can be rewritten as $(\mathbf{U}\mathbf{\Sigma}_k^{1/2})(\mathbf{\Sigma}_k^{1/2}\mathbf{V}^\top)$, reducing parameters from mn to $k(m+n)$.

Fisher Information Following empirical approximation, the (empirical) FIM used in our paper is computed as

$$\mathbf{F}_Z = \frac{1}{N_{\text{cal}}} \sum_{i=1}^{N_{\text{cal}}} \mathbf{g}_i \mathbf{g}_i^\top, \quad \mathbf{g}_i = \nabla_{\mathbf{Z}_i} \mathcal{L}(\mathbf{Z}_i). \quad (12)$$

where N_{cal} is the number of calibration samples.

A.2 From Base Objective to Trace Formulation

Starting from the compression objective in Equation 4 in the main paper, we optimize

$$\min_{\mathbf{W}'} (1 - \alpha) \mathbb{E} [\|\mathbf{L}(\mathbf{W}\mathbf{X} - \mathbf{W}'\mathbf{X})\|_2^2] + \alpha \mathbb{E} [\|\mathbf{L}(\mathbf{W}\mathbf{X} - \mathbf{W}'\mathbf{X}')\|_2^2], \quad (13)$$

where \mathbf{X} denotes the clean input activation, \mathbf{X}' is the shifted activation induced by previously compressed layers, and \mathbf{L} is decomposed from \mathbf{F}_Z (Equation 12), *i.e.* $\mathbf{F}_Z = \mathbf{L}^\top \mathbf{L}$. \mathbf{W} and \mathbf{W}' are the original and compressed weights, respectively. Note that the expectation $\mathbb{E}[\cdot]$ is taken over the data distribution. Therefore, the activations \mathbf{X} and \mathbf{X}' are random variables, while \mathbf{W} , \mathbf{W}' , and \mathbf{L} which is estimated over the entire calibration set, are deterministic constants with respect to this expectation. The first term captures intra-layer reconstruction error under clean inputs, while the second term models propagated error caused by preceding layer compression.

For a single-sample vector \mathbf{a} , we use

$$\|\mathbf{a}\|_2^2 = \text{Tr}(\mathbf{a}\mathbf{a}^\top). \quad (14)$$

For the first term, using the linearity of the trace operator and the deterministic nature of \mathbf{L} , \mathbf{W} , and \mathbf{W}' , we can move the expectation inside:

$$\begin{aligned} \mathbb{E}[\|\mathbf{L}(\mathbf{W}\mathbf{X} - \mathbf{W}'\mathbf{X})\|_2^2] &= \mathbb{E} [\text{Tr} (\mathbf{L}(\mathbf{W}\mathbf{X} - \mathbf{W}'\mathbf{X})(\mathbf{W}\mathbf{X} - \mathbf{W}'\mathbf{X})^\top \mathbf{L}^\top)] \\ &= \mathbb{E} [\text{Tr} (\mathbf{L}(\mathbf{W} - \mathbf{W}')\mathbf{X}\mathbf{X}^\top (\mathbf{W} - \mathbf{W}')^\top \mathbf{L}^\top)] \\ &= \text{Tr} (\mathbf{L}(\mathbf{W} - \mathbf{W}')\mathbb{E}[\mathbf{X}\mathbf{X}^\top](\mathbf{W} - \mathbf{W}')^\top \mathbf{L}^\top). \end{aligned} \quad (15)$$

Let $\mathbf{\Sigma}_{\mathbf{X}\mathbf{X}} = \mathbb{E} [\mathbf{X}\mathbf{X}^\top]$, then expanding the quadratic form gives

$$\begin{aligned} \mathbb{E}[\|\mathbf{L}(\mathbf{W}\mathbf{X} - \mathbf{W}'\mathbf{X})\|_2^2] &= \text{Tr}(\mathbf{L}\mathbf{W}\mathbf{\Sigma}_{\mathbf{X}\mathbf{X}}\mathbf{W}^\top \mathbf{L}^\top) - \text{Tr}(\mathbf{L}\mathbf{W}\mathbf{\Sigma}_{\mathbf{X}\mathbf{X}}\mathbf{W}'^\top \mathbf{L}^\top) \\ &\quad - \text{Tr}(\mathbf{L}\mathbf{W}'\mathbf{\Sigma}_{\mathbf{X}\mathbf{X}}\mathbf{W}^\top \mathbf{L}^\top) + \text{Tr}(\mathbf{L}\mathbf{W}'\mathbf{\Sigma}_{\mathbf{X}\mathbf{X}}\mathbf{W}'^\top \mathbf{L}^\top), \end{aligned} \quad (16)$$

Since $\text{Tr}(\mathbf{L}\mathbf{W}\Sigma_{\mathbf{X}\mathbf{X}}\mathbf{W}^\top\mathbf{L}^\top)$ is independent to \mathbf{W}' and using transpose invariance of the trace $\text{Tr}(\mathbf{A}) = \text{Tr}(\mathbf{A}^\top)$, we simplify:

$$\mathbb{E} [\|\mathbf{L}(\mathbf{W}\mathbf{X} - \mathbf{W}'\mathbf{X})\|_2^2] = \text{const} - 2\text{Tr}(\mathbf{L}\mathbf{W}'\Sigma_{\mathbf{X}\mathbf{X}}\mathbf{W}^\top\mathbf{L}^\top) + \text{Tr}(\mathbf{L}\mathbf{W}'\Sigma_{\mathbf{X}\mathbf{X}}\mathbf{W}'^\top\mathbf{L}^\top). \quad (17)$$

Similarly, the second term can be expressed as

$$\mathbb{E} [\|\mathbf{L}(\mathbf{W}\mathbf{X} - \mathbf{W}'\mathbf{X}')\|_2^2] = \text{const} - 2\text{Tr}(\mathbf{L}\mathbf{W}'\Sigma_{\mathbf{X}'\mathbf{X}}\mathbf{W}^\top\mathbf{L}^\top) + \text{Tr}(\mathbf{L}\mathbf{W}'\Sigma_{\mathbf{X}'\mathbf{X}}\mathbf{W}'^\top\mathbf{L}^\top), \quad (18)$$

where

$$\Sigma_{\mathbf{X}'\mathbf{X}} = \mathbb{E}[\mathbf{X}'\mathbf{X}^\top], \quad \Sigma_{\mathbf{X}'\mathbf{X}'} = \mathbb{E}[\mathbf{X}'\mathbf{X}'^\top].$$

Substituting Equation 17 and Equation 18 into Equation 13 and collecting all terms that depend on \mathbf{W}' , we obtain

$$\min_{\mathbf{W}'} (1 - \alpha)\mathbb{E} [\|\mathbf{L}(\mathbf{W}\mathbf{X} - \mathbf{W}'\mathbf{X})\|_2^2] + \alpha\mathbb{E} [\|\mathbf{L}(\mathbf{W}\mathbf{X} - \mathbf{W}'\mathbf{X}')\|_2^2] \quad (19)$$

$$= \min_{\mathbf{W}'} -2\text{Tr}(\mathbf{L}\mathbf{W}'\Sigma_{\text{cov}}\mathbf{W}^\top\mathbf{L}^\top) + \text{Tr}(\mathbf{L}\mathbf{W}'\Sigma_{\text{c_cov}}\mathbf{W}'^\top\mathbf{L}^\top) + \text{const}, \quad (20)$$

with covariance matrices

$$\Sigma_{\text{cov}} = (1 - \alpha)\Sigma_{\mathbf{X}\mathbf{X}} + \alpha\Sigma_{\mathbf{X}'\mathbf{X}}, \quad \Sigma_{\text{c_cov}} = (1 - \alpha)\Sigma_{\mathbf{X}\mathbf{X}} + \alpha\Sigma_{\mathbf{X}'\mathbf{X}'}. \quad (21)$$

This is the trace-equivalent form used in Equation 5 of the main paper. It integrates intra-layer reconstruction perturbation, and propagated compression error into a single unified objective.

A.3 From Trace Formulation to Frobenius-norm

To obtain a tractable solver, we convert Equation 19 into a standard low-rank regression problem. In practice, $\Sigma_{\text{c_cov}}$ is positive definite Appendix E.3, allowing a Cholesky decomposition $\Sigma_{\text{c_cov}} = \mathbf{R}\mathbf{R}^\top$. Substituting this factorization into the second term in Equation 19 yields:

$$\text{Tr}(\mathbf{L}\mathbf{W}'\mathbf{R}\mathbf{R}^\top\mathbf{W}'^\top\mathbf{L}^\top) = \text{Tr}(\mathbf{L}\mathbf{W}'\mathbf{R}(\mathbf{L}\mathbf{W}'\mathbf{R})^\top). \quad (22)$$

For the first term in Equation 19, we rearrange it

$$\begin{aligned} -2\text{Tr}(\mathbf{L}\mathbf{W}'\Sigma_{\text{cov}}\mathbf{W}^\top\mathbf{L}^\top) &= -2\text{Tr}(\mathbf{L}\mathbf{W}'\mathbf{R}\mathbf{R}^{-1}\Sigma_{\text{cov}}\mathbf{W}^\top\mathbf{L}^\top) \\ &= -2\text{Tr}((\mathbf{R}^{-1}\Sigma_{\text{cov}}\mathbf{W}^\top\mathbf{L}^\top)(\mathbf{L}\mathbf{W}'\mathbf{R})) \\ &= -2\text{Tr}((\mathbf{L}\mathbf{W}'\Sigma_{\text{cov}}^\top\mathbf{R}^{-\top})^\top(\mathbf{L}\mathbf{W}'\mathbf{R})). \end{aligned} \quad (23)$$

For any matrices \mathbf{A} and \mathbf{B} of compatible dimensions, the following holds:

$$\|\mathbf{A} - \mathbf{B}\|_F^2 = \text{Tr}(\mathbf{A}\mathbf{A}^\top) - 2\text{Tr}(\mathbf{B}^\top\mathbf{A}) + \|\mathbf{B}\|_F^2. \quad (24)$$

We define

$$\mathbf{A} = \mathbf{L}\mathbf{W}'\mathbf{R}, \quad \mathbf{B} = \mathbf{L}\mathbf{W}'\Sigma_{\text{cov}}^\top\mathbf{R}^{-\top}.$$

Since $\|\mathbf{B}\|_F^2$ does not depend on \mathbf{W}' , it can be absorbed into the const term, allowing us to rewrite the objective as:

$$\min_{\mathbf{W}'} \|\mathbf{L}\mathbf{W}'\mathbf{R} - \mathbf{L}\mathbf{W}'\Sigma_{\text{cov}}^\top\mathbf{R}^{-\top}\|_F^2. \quad (25)$$

This objective is exactly the same as Equation 7 in the main paper.

A.4 Derivation of Loss Degradation Derivation in Rank Selection

As derived from Equation 2, the impact of the perturbation $\Delta\mathbf{Z}$ on the final loss can be approximated by the objective:

$$\mathbb{E}[\Delta\mathcal{L}] \approx \mathbb{E} [\|\mathbf{L}\Delta\mathbf{Z}\|_2^2]. \quad (26)$$

If we strictly consider the clean input condition (i.e., isolating the current layer by assuming no upstream errors, $\mathbf{X}' = \mathbf{X}$), the perturbation simplifies to $\Delta\mathbf{Z} = (\mathbf{W} - \mathbf{W}')\mathbf{X}$. Let $\mathbf{A} = \mathbf{L}(\mathbf{W} - \mathbf{W}')$ for brevity. We expand the expected squared norm:

$$\mathbb{E} [\|\mathbf{A}\mathbf{X}\|_2^2] = \mathbb{E} [\text{tr}(\mathbf{A}\mathbf{X}\mathbf{X}^\top\mathbf{A}^\top)] = \text{tr}(\mathbf{A}\mathbb{E}[\mathbf{X}\mathbf{X}^\top]\mathbf{A}^\top) = \text{tr}(\mathbf{A}\Sigma_{\mathbf{X}\mathbf{X}}\mathbf{A}^\top). \quad (27)$$

Recalling that the input covariance is decomposed as $\Sigma_{\mathbf{X}\mathbf{X}} = \mathbf{R}^c \mathbf{R}^{c\top}$, we substitute and apply the identity $\text{tr}(\mathbf{B}\mathbf{B}^\top) = \|\mathbf{B}\|_F^2$:

$$\text{tr}(\mathbf{A} \mathbf{R}^c \mathbf{R}^{c\top} \mathbf{A}^\top) = \text{tr}((\mathbf{A} \mathbf{R}^c)(\mathbf{A} \mathbf{R}^c)^\top) = \|\mathbf{A} \mathbf{R}^c\|_F^2 = \|\mathbf{L} \mathbf{W} \mathbf{R}^c - \mathbf{L} \mathbf{W}' \mathbf{R}^c\|_F^2. \quad (28)$$

Thus under clean input condition, the loss change can be approximated:

$$\mathbb{E}[\Delta \mathcal{L}] \approx \mathbb{E}[\|\mathbf{L}(\mathbf{W} - \mathbf{W}')\mathbf{X}\|_2^2] = \|\mathbf{L} \mathbf{W} \mathbf{R}^c - \mathbf{L} \mathbf{W}' \mathbf{R}^c\|_F^2. \quad (29)$$

Let $\mathbf{M}^* = \mathbf{L} \mathbf{W} \mathbf{R}^c$ and $\mathbf{M} = \mathbf{L} \mathbf{W}' \mathbf{R}^c$. The compression objective becomes a standard low-rank approximation problem:

$$\min_{\mathbf{M}} \|\mathbf{M} - \mathbf{M}^*\|_F^2 \quad \text{subject to} \quad \text{rank}(\mathbf{M}) = k. \quad (30)$$

By the Eckart–Young–Mirsky theorem, the optimal solution is the rank- k truncated SVD of \mathbf{M}^* . Writing $\mathbf{M}^* = \mathbf{U} \Sigma \mathbf{V}^\top$, if we decide to retain the top- k ranks, the residual error equals the sum of the squared singular values beyond rank k . Thus, the approximated loss degradation is:

$$\mathbb{E}[\Delta \mathcal{L}] \approx \mathbb{E}[\|\mathbf{L}(\mathbf{W} - \mathbf{W}')\mathbf{X}\|_2^2] = \sum_{i=k+1}^r \sigma_i^2. \quad (31)$$

where r denotes the full rank of the transformed matrix, *i.e.* $r = \text{rank}(\mathbf{M}^*) = \text{rank}(\mathbf{W})$ and σ_i is its i -th singular value. Consequently, each squared singular value σ_i^2 quantifies the final loss degradation that would occur if the i -th singular component is dropped. This provides a unified, globally comparable effect across all heterogeneous layers, *i.e.* all linear layers can be compared under the same evaluation.

B Additional Experimental Results

B.1 Quantitative Results

We provide fully detailed experimental results. For all comparisons, we tested compression ratios 1.0, 0.8, 0.6, 0.4, and 0.2. Some results are presented in the main paper, but we still list them for the purpose of easy comparisons.

B.1.1 Comparisons on Poseidon

The results on the additional datasets, as shown in Table 4, further solidify the robustness and generalizability of our proposed method across diverse physical domains. Across all three scenarios—NS-BB, CE-RPUI, and Wave-Layer—our method consistently maintains a significant lead over all baselines. While traditional SVD-based approaches typically experience catastrophic performance collapse (with errors frequently exceeding 100% or even 1000%) as soon as the compression ratio drops below 0.8, our method keeps the error near-zero at moderate compression and preserves physical validity even at the extreme 0.2 ratio.

NS-BB In the Navier-Stokes Brownian Bridge(NS-BB) scenario, which involves complex multi-scale eddy structures, our method demonstrates exceptional adherence to physical constraints. Even at the most aggressive compression ratio of 0.2, the divergence-free (Div-Free) and vorticity errors remain remarkably low at **0.29%** and **0.77%**, respectively. This indicates that our approach effectively captures the underlying conservation laws and local fluid dynamics, preventing the accumulation of unphysical artifacts that plague baseline methods.

CE-RPUI The Compressible Euler Riemann-Kelvin-Helmholtz (CE-RPUI) task presents a significant challenge due to its shock-driven turbulent mixing and sensitivity to interface discontinuities. Our method exhibits high robustness in this regime; at a 0.4 ratio, the degradation remains negligible, and even at the 0.2 limit, the Base Loss is contained at **4.50%**. In contrast, baseline methods like ASVD and SAES-SVD fail to maintain the integrity of the shock fronts, resulting in errors that are orders of magnitude higher.

Table 4: Rest Experimental Results on Poseidon.

Poseidon	Size	NS-BB				CE-RPUI		Wave-Layer			
		Base Loss ↓	Sobolev ↓	Div-Free ↓	Vorticity ↓	Base Loss ↓	Sobolev ↓	Base Loss ↓	Sobolev ↓		
1	Origin	628.6M	0.00%	0.00%	0.00%	0.00%	0.00%	0.00%	0.00%		
0.8	ASVD	502.8M	1239%	961.8%	383.5%	1260%	66.56%	16.26%	53.87%	1946%	
	FWSVD	502.7M	5929%	3264%	1440%	4073%	398.4%	70.72%	879.8%	9019%	
	SVD-LLM V2	522.9M	5793%	3495%	1742%	4061%	416.4%	53.06%	877.0%	7754%	
	Dobi-SVD	503.7M	6974%	6974%	3400%	1322%	4242%	480.8%	97.35%	1004%	11207%
	SAES-SVD	502.7M	2254%	2235%	1297%	1801%	185.2%	45.63%	336.4%	5012%	
	Ours	503.0M	0.00%	0.00%	0.00%	0.00%	0.00%	0.00%	0.00%	0.00%	
0.6	ASVD	377.0M	3763%	3695%	1785%	3176%	324.8%	58.16%	386.9%	11953%	
	FWSVD	377.1M	6121%	4058%	1775%	4148%	413.2%	118.8%	903.7%	10956%	
	SVD-LLM V2	424.8M	6904%	3677%	1797%	4353%	441.7%	121.3%	892.6%	10578%	
	Dobi-SVD	378.1M	6785%	4128%	1718%	4258%	527.1%	116.9%	1025%	9618%	
	SAES-SVD	377.1M	2480%	2372%	1372%	1992%	198.9%	56.34%	324.5%	6126%	
	Ours	377.5M	0.00%	0.01%	0.01%	0.01%	0.04%	0.02%	0.01%	0.01%	
0.4	ASVD	251.4M	4691%	6606%	2967%	3998%	441.4%	207.9%	627.5%	22672%	
	FWSVD	251.5M	7133%	7037%	2926%	4383%	446.1%	323.2%	940.5%	14994%	
	SVD-LLM V2	321.6M	7242%	5031%	2371%	4455%	491.2%	280.1%	1021%	28063%	
	Dobi-SVD	252.6M	9064%	7041%	3003%	4564%	511.0%	186.6%	1037%	22288%	
	SAES-SVD	251.5M	2641%	2535%	1486%	2095%	213.4%	72.77%	324.1%	6886%	
	Ours	251.9M	0.10%	0.05%	0.01%	0.08%	0.15%	0.14%	0.07%	0.31%	
0.2	ASVD	125.8M	6179%	8106%	3484%	4777%	534.9%	555.4%	721.2%	22274%	
	FWSVD	125.9M	7644%	11629%	4266%	4761%	523.6%	592.4%	1047%	25799%	
	SVD-LLM V2	202.7M	8190%	6519%	3020%	4701%	623.8%	288.4%	1719%	27723%	
	Dobi-SVD	127.0M	7138%	11119%	2838%	4902%	582.3%	364.8%	2447%	26380%	
	SAES-SVD	125.9M	3383%	3349%	1914%	2692%	270.0%	96.17%	504.9%	9305%	
	Ours	126.3M	1.20%	0.83%	0.29%	0.77%	4.50%	8.33%	0.92%	41.07%	

Wave-Layer For the Wave-Layer dataset, which simulates wave propagation through stratified media, the results reinforce our observations regarding wave-dominated physics. As with the Wave-Gaussian task in the main text, the Sobolev Loss shows greater sensitivity at extreme compression (reaching **41.07%** at ratio 0.2), which is characteristic of the phase-shift accumulation inherent in globally coherent propagating modes. However, compared to the closest baseline (SAES-SVD) which reaches a staggering **9305%** error, our method provides a vastly more stable and physically meaningful approximation of the wave operator.

B.1.2 Comparisons on MPP

We further evaluate our method on MPP, another unified multi-physics foundation model, across four scenarios: Incompressible Naiver Stoke, Compressible Naiver Stoke, Diffusion-Reaction, and Shallow Water, with results reported in Table 5.

Consistent with the VICON results, both Ours variants outperform all baselines across compression ratios, demonstrating that the proposed framework generalizes well to unified multi-physics pretraining models. Under mild and moderate compression (ratios 0.8 and 0.6), our methods remain close to the original model on most metrics, while competing baselines already exhibit substantial degradation. At higher compression levels (ratios 0.4 and 0.2), the advantage becomes more pronounced. Several baselines deteriorate sharply, especially on more challenging scenarios such as Shallow Water and Diff React 2D. For example, at ratio 0.2 on Shallow Water, DobiSVD increases Base Loss by 27, 244.64%, whereas Ours and Ours* limit the increase to 5, 250.31% and 1, 330.00%, respectively. Similar trends are observed on Sobolev Loss and other metrics.

B.1.3 Main Paper Full Results on Poseidon and VICON

Also, the results of VICON, and NS-PwC, CE-RM and Wave-Gaussian (containing 0.8 compression ratio) on Poseidon are shown in Table 7 and Table 6 respectively.

B.2 Qualitative Results

CE-RM Figure 3 compares predicted physical fields (ρ, u, v, p) on the CE-RM (Compressible Euler–Richtmyer–Meshkov) dataset. This dataset is characterized by high-Mach shock waves and complex interfacial instabilities that produce sharp discontinuities and intricate mushroom filament structures in the density field.

Table 5: Experimental Results on MPP.

MPP	Size	IncompNS				CompNS		DiffRe-2D		SWE		
		Base Loss ↓	Sobolev ↓	Div-Free ↓	Vorticity ↓	Base Loss ↓	Sobolev ↓	Base Loss ↓	Sobolev ↓	Base Loss ↓	Sobolev ↓	
1	Origin	407.1M	0.00%	0.00%	0.00%	0.00%	0.00%	0.00%	0.00%	0.00%	0.00%	
0.8	ASVD	366.7M	2003%	72.38%	0.71%	193.6%	4.65%	0.73%	290.0%	59.07%	531.6%	75.38%
	FWSVD	366.7M	678.8%	46.03%	0.19%	97.37%	2.15%	0.65%	66.93%	23.12%	288.2%	52.56%
	SVD-LLM V2	366.8M	29.15%	2.05%	0.10%	6.29%	0.86%	0.05%	25.95%	5.96%	45.31%	7.53%
	Dobi-SVD	367.0M	485.1%	49.66%	0.18%	86.45%	0.68%	0.06%	60.93%	24.78%	244.7%	42.97%
	SAES-SVD	366.7M	25.08%	2.00%	0.09%	4.76%	0.98%	0.04%	25.98%	6.35%	56.51%	8.93%
	Ours	366.8M	28.24%	2.84%	0.12%	5.22%	0.26%	0.01%	19.35%	4.28%	70.33%	8.05%
	Ours*	366.8M	16.83%	1.55%	0.09%	3.04%	0.04%	0.06%	3.06%	0.88%	17.22%	2.28%
0.6	ASVD	326.4M	9434%	283.6%	6.28%	593.0%	64.25%	6.62%	2412%	210.9%	4836%	380.5%
	FWSVD	326.4M	3168%	124.6%	1.60%	262.5%	6.05%	1.68%	242.8%	61.44%	1311%	180.1%
	SVD-LLM V2	326.5M	171.8%	10.84%	0.32%	29.86%	4.36%	0.74%	131.4%	25.14%	297.9%	42.67%
	Dobi-SVD	326.7M	4148%	207.1%	3.28%	322.8%	9.04%	1.21%	292.9%	70.01%	1851%	189.4%
	SAES-SVD	326.4M	122.9%	8.91%	0.28%	19.62%	4.84%	0.34%	113.3%	22.36%	278.2%	39.82%
	Ours	326.5M	159.6%	15.04%	0.34%	28.12%	0.51%	0.11%	120.8%	19.17%	259.6%	32.76%
	Ours*	326.5M	92.62%	9.14%	0.26%	17.87%	2.05%	0.46%	13.60%	3.23%	71.55%	9.14%
0.4	ASVD	286.1M	10245%	296.4%	7.04%	617.6%	72.55%	9.63%	2524%	216.1%	7345%	474.7%
	FWSVD	286.1M	9589%	297.9%	8.97%	584.5%	24.04%	5.18%	878.8%	153.2%	12771%	738.1%
	SVD-LLM V2	286.3M	803.5%	39.36%	0.86%	100.5%	24.64%	3.63%	440.7%	65.71%	1251%	137.1%
	Dobi-SVD	286.3M	14059%	700.7%	25.47%	1010%	53.01%	8.07%	1238%	181.2%	17117%	729.3%
	SAES-SVD	286.1M	581.9%	31.47%	0.76%	81.94%	23.37%	2.17%	377.1%	57.16%	1114%	122.3%
	Ours	286.3M	718.2%	56.43%	0.99%	96.92%	6.09%	1.23%	460.2%	59.68%	1188%	117.3%
	Ours*	286.3M	419.2%	38.14%	0.71%	70.39%	12.64%	2.73%	62.80%	11.25%	285.3%	36.63%
0.2	ASVD	245.8M	12273%	395.7%	10.74%	806.0%	105.0%	18.32%	2854%	241.8%	19920%	849.4%
	FWSVD	245.8M	30072%	1129%	47.16%	1646%	109.5%	18.32%	3682%	422.7%	29702%	1333%
	SVD-LLM V2	246.0M	3182%	118.5%	1.78%	215.8%	124.8%	15.00%	1376%	138.7%	3203%	282.8%
	Dobi-SVD	245.9M	75128%	2257%	116.7%	3082%	371.4%	47.83%	9277%	713.8%	27218%	1350%
	SAES-SVD	245.8M	2362%	95.69%	1.90%	185.6%	102.6%	9.62%	1264%	125.8%	3308%	268.8%
	Ours	246.0M	2956%	175.7%	2.90%	245.7%	43.68%	7.87%	1514%	144.2%	5488%	352.4%
	Ours*	246.0M	1929%	137.8%	2.20%	202.6%	94.22%	12.93%	317.5%	42.87%	1299%	134.8%

Table 6: Experimental Results on Poseidon

Poseidon	Size	NS-PwC				CE-RM		Wave-Gauss		
		Base Loss ↓	Sobolev ↓	Div-Free ↓	Vorticity ↓	Base Loss ↓	Sobolev ↓	Base Loss ↓	Sobolev ↓	
1	Origin	628.6M	0.00%	0.00%	0.00%	0.00%	0.00%	0.00%	0.00%	
0.8	ASVD	502.9M	2000%	884.6%	498.7%	1486%	9.01%	1.79%	81.85%	1090%
	FWSVD	502.7M	6930%	2276%	1345%	3657%	20.72%	0.50%	559.6%	1779%
	SVD-LLM V2	524.2M	6851%	1781%	1102%	3602%	22.81%	4.34%	556.6%	1256%
	Dobi-SVD	503.7M	7961%	2163%	1283%	3790%	34.17%	5.31%	632.9%	2202%
	SAES-SVD	502.7M	2616%	1653%	1464%	1670%	1.07%	1.13%	229.9%	2438%
	Ours	503.0M	0.00%	0.00%	0.00%	0.00%	0.00%	0.00%	0.00%	0.00%
0.6	ASVD	376.9M	4496%	2680%	2017%	2805%	25.39%	6.61%	352.1%	6202%
	FWSVD	377.1M	7124%	2977%	1700%	3727%	23.24%	8.51%	569.7%	2415%
	SVD-LLM V2	438.3M	7038%	2449%	1482%	3651%	26.78%	9.31%	576.4%	4982%
	Dobi-SVD	378.1M	7468%	3036%	2137%	3719%	35.70%	24.58%	658.6%	9210%
	SAES-SVD	377.1M	2882%	1763%	1572%	1863%	2.19%	2.53%	225.8%	3354%
	Ours	377.5M	0.00%	0.01%	0.00%	0.01%	0.00%	0.00%	0.00%	0.01%
0.4	ASVD	251.4M	5169%	4364%	2773%	3311%	34.10%	15.79%	475.4%	14572%
	FWSVD	251.5M	7846%	5080%	2449%	3961%	28.33%	28.64%	588.1%	3542%
	SVD-LLM V2	374.9M	8741%	6051%	4530%	4131%	35.87%	54.99%	656.0%	19627%
	Dobi-SVD	252.6M	8481%	5206%	2709%	4048%	39.27%	25.91%	670.4%	10497%
	SAES-SVD	251.5M	3062%	1868%	1632%	1967%	3.46%	6.18%	249.3%	4020%
	Ours	251.9M	0.26%	0.08%	0.03%	0.17%	0.01%	0.05%	0.04%	0.40%
0.2	ASVD	125.8M	6725%	6183%	3563%	4167%	41.02%	80.05%	525.0%	13007%
	FWSVD	125.9M	8622%	7650%	3770%	4276%	40.57%	97.34%	655.1%	11452%
	SVD-LLM V2	353.2M	9529%	6011%	4183%	4434%	61.44%	66.29%	1122%	19865%
	Dobi-SVD	127.0M	8774%	10090%	4999%	4440%	44.78%	29.72%	728.6%	20124%
	SAES-SVD	125.9M	3726%	2429%	2199%	2426%	6.25%	9.83%	366.9%	5873%
	Ours	126.3M	2.64%	1.79%	0.52%	1.35%	0.10%	1.01%	0.70%	151.9%

ASVD, FWSVD, SVD-LLM V2, and Dobi-SVD suffer from near-complete information collapse; their predictions are largely featureless, failing to capture even the most basic macroscopic structures. SAES-SVD recovers the global symmetry of the expanding flow but significantly blurs the sharp discontinuities and lacks the high-frequency components needed to resolve fine-scale shock reflections. Our method, by contrast, demonstrates remarkable visual consistency with the original model across all physical variables, preserving the sharp shock fronts, the Richtmyer–Meshkov mushroom structures in the density field, and the complex wave interference patterns in the velocity and pressure fields even at $t=15$.

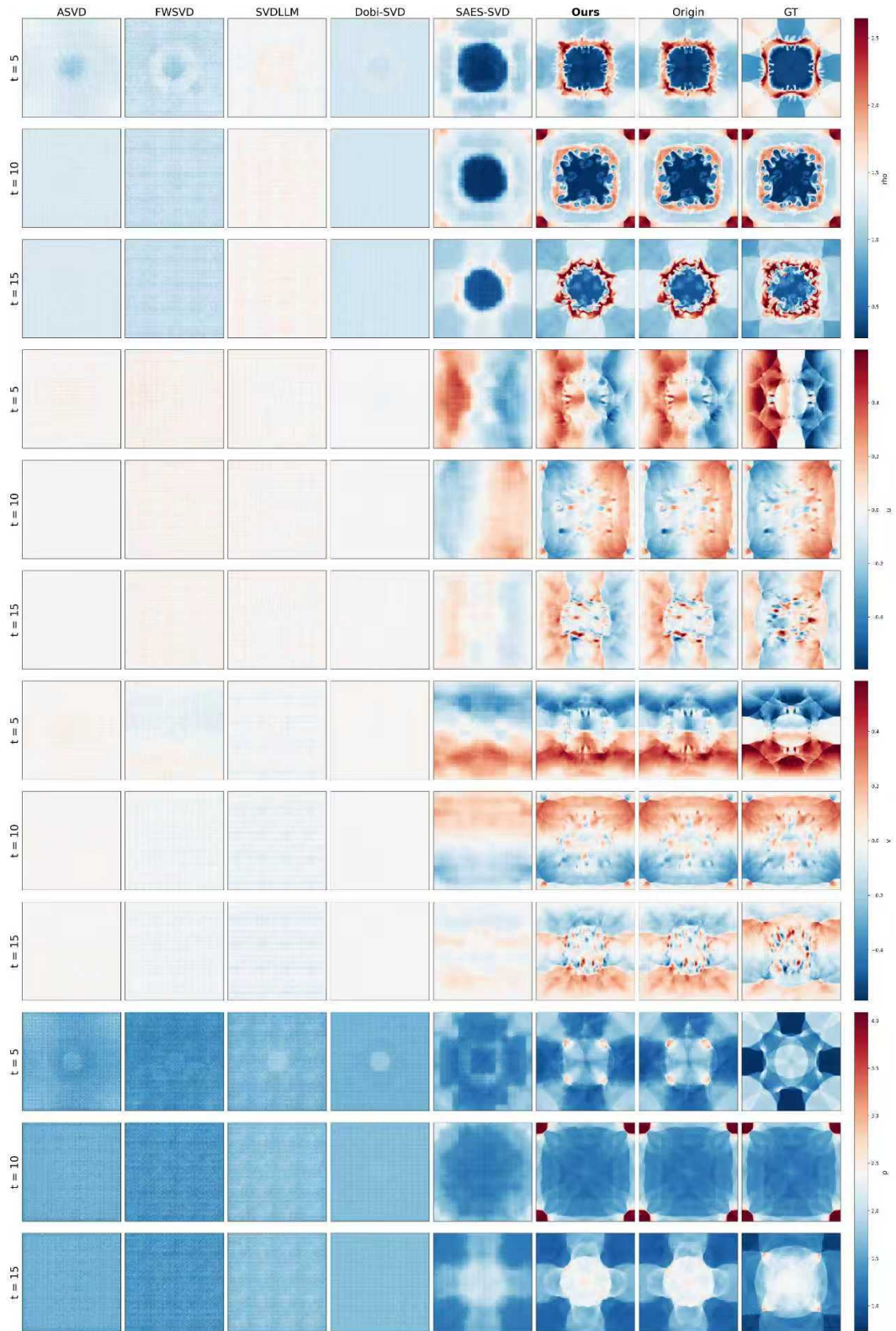


Figure 3: Predicted physical fields (ρ, u, v, p) on the CE-RM dataset at compression ratio 0.2 over three rollout horizons ($t = 5, 10, 15$).

Table 7: Experimental Results on VICON.

VICON	Size	NS-2D				Comp-2D		Euler-2D		
		Base Loss ↓	Sobolev ↓	Div-Free ↓	Vorticity ↓	Base Loss ↓	Sobolev ↓	Base Loss ↓	Sobolev ↓	
1	Origin	87.8M	0.00%	0.00%	0.00%	0.00%	0.00%	0.00%	0.00%	
0.8	ASVD	70.1M	1922%	48.48%	18.58%	184.9%	14247%	317.2%	1219%	30.49%
	FWSVD	70.3M	1011%	253.7%	14.36%	302.3%	2859%	748.3%	276.4%	12.23%
	SVD-LLM V2	70.2M	16.64%	2.92%	1.90%	11.08%	65.11%	22.19%	16.27%	1.00%
	Dobi-SVD	69.1M	1762%	108.3%	16.06%	147.0%	277.9%	230.4%	66.02%	21.04%
	SAES-SVD	70.3M	15.15%	3.44%	1.48%	9.90%	52.18%	19.86%	10.04%	8.99%
	Ours	70.3M	4.61%	1.07%	0.51%	1.92%	6.17%	5.40%	4.14%	29.26%
	Ours*	70.3M	0.58%	0.35%	0.32%	0.02%	0.75%	0.85%	2.55%	29.00%
0.6	ASVD	52.4M	10140%	528.7%	7.01%	476.1%	41318%	1394%	2692%	97.36%
	FWSVD	52.7M	1861%	302.3%	2.23%	357.5%	7885%	947.6%	805.1%	57.72%
	SVD-LLM V2	52.7M	73.76%	11.74%	5.30%	43.87%	260.0%	60.00%	47.26%	3.31%
	Dobi-SVD	52.9M	1968%	109.3%	24.08%	163.6%	757.4%	260.1%	128.6%	18.49%
	SAES-SVD	52.7M	49.63%	7.06%	3.92%	26.01%	144.7%	33.70%	36.66%	25.99%
	Ours	52.8M	2.07%	1.22%	0.21%	3.08%	16.54%	3.82%	3.08%	28.35%
	Ours*	52.8M	0.51%	0.02%	0.71%	0.06%	18.05%	10.86%	8.52%	28.89%
0.4	ASVD	33.5M	13064%	532.5%	11.34%	490.4%	46290%	1382%	2865%	94.70%
	FWSVD	35.2M	4862%	349.7%	3.24%	437.5%	22440%	1155%	2010%	69.01%
	SVD-LLM V2	35.7M	689.5%	32.06%	10.96%	136.1%	2152%	163.9%	265.6%	16.69%
	Dobi-SVD	37.0M	2607%	113.3%	34.70%	209.6%	1795%	285.9%	278.3%	13.58%
	SAES-SVD	35.2M	156.3%	18.10%	8.68%	68.40%	609.3%	74.10%	115.5%	20.65%
	Ours	35.3M	24.98%	4.23%	0.85%	11.32%	127.4%	26.40%	27.05%	26.91%
	Ours*	35.3M	18.92%	2.90%	1.30%	7.26%	81.80%	29.87%	26.11%	27.55%
0.2	ASVD	16.5M	15583%	535.6%	12.51%	484.5%	48919%	1392%	3016%	94.46%
	FWSVD	17.7M	11265%	295.8%	29.67%	462.3%	43908%	1232%	2769%	66.10%
	SVD-LLM V2	18.3M	2245%	67.19%	40.38%	290.2%	16822%	399.9%	1230%	34.89%
	Dobi-SVD	20.2M	3705%	118.8%	46.52%	262.2%	4929%	358.1%	630.2%	7.02%
	SAES-SVD	17.7M	651.3%	37.96%	16.22%	165.2%	2952%	169.7%	432.3%	12.12%
	Ours	17.8M	291.1%	23.19%	7.87%	76.27%	1051%	99.28%	291.8%	16.10%
	Ours*	17.8M	239.7%	20.17%	8.07%	66.31%	927.2%	116.8%	248.3%	17.75%

C Experiment Setting Details

C.1 Calibration Dataset

Our calibration dataset consists of 13,440 samples (210 samples/per trajectory \times 64 trajectories) for the Incompressible Navier-Stokes and Compressible Euler tasks, and 7,680 samples (120 samples/trajectory \times 64 trajectories) for the Wave Equation. The sample counts per trajectory are derived from the summation of time steps up to the final sampled time:

$$N = \sum_{i=1}^{T_{final}} i, \quad (32)$$

where $T_{final} = 20$ for Navier-Stokes and Euler tasks ($N = 210$), and $T_{final} = 15$ for the Wave Equation ($N = 120$). Furthermore, we include 1,028 samples for VICON and 16 samples for MPP per physical scenario. These configurations were selected to provide an optimal trade-off between the preservation of model fidelity and overall compression efficiency.

C.2 Test Dataset

We evaluate on three benchmarks: Poseidon, VICON, and MPP. For Poseidon, we test all trajectories by considering every ordered snapshot pair (x_i, x_j) within each sequence with $t_i < t_j$, thereby covering both short- and long-range temporal dynamics. For VICON, we use the default test split and evaluate snapshot prediction over all available samples. For MPP, where only a validation dataset is provided, we use the validation split for evaluation and test up to 64 trajectories per sub-dataset. Evaluation spans multiple physical regimes, including incompressible and compressible flows.

C.3 Evaluation Metrics

This part provides detailed definitions of the metrics used to evaluate compression quality. As stated in the main paper, all reported values are expressed as absolute percentage changes relative to the uncompressed model. We group the metrics into two categories: (i) model base loss and Sobolev

loss, which measure predictive fidelity and smoothness, and (ii) physics-specific quantities that assess structural consistency of the solution fields, such as divergence-free error for incompressible Navier–Stokes systems.

Model Base Loss. The model base loss measures agreement between the model prediction and the ground-truth target under the original training objective. Let $f_\theta(\mathbf{z})$ denote the model prediction for input \mathbf{z} , and let \mathbf{y} be the corresponding target. We evaluate the empirical loss over the test set $\mathcal{D}_{\text{test}}$:

$$\mathcal{L}_{\text{base}} = \frac{1}{|\mathcal{D}_{\text{test}}|} \sum_{(\mathbf{z}, \mathbf{y}) \in \mathcal{D}_{\text{test}}} \ell(f_\theta(\mathbf{z}), \mathbf{y}), \quad (33)$$

where $\ell(\cdot, \cdot)$ is the task-specific criterion used during training. In practice, Poseidon uses relative l_1 error, VICON uses mean squared error (MSE), and MPP uses relative MSE.

Sobolev Loss. To evaluate functional smoothness and derivative consistency across different orders, we introduce a Sobolev-type loss. Let \mathbf{u} denote the reference field and $\hat{\mathbf{u}}$ the model prediction on the discrete spatial grid Ω_h . The loss compares their finite-difference derivatives up to order p using either l_1 or l_2 :

$$\mathcal{L}_{\text{Sob}}^{(q)} = \sum_{|\alpha| \leq p} \lambda_\alpha \frac{1}{|\Omega_h|} \sum_{\mathbf{r} \in \Omega_h} \|D^\alpha \mathbf{u}(\mathbf{r}) - D^\alpha \hat{\mathbf{u}}(\mathbf{r})\|_q^q, \quad q \in \{1, 2\}. \quad (34)$$

Here, D^α denotes the finite-difference approximation of the spatial derivative indexed by the multi-index α , and p is the highest derivative order included. The coefficient λ_α controls the contribution of each derivative term, balancing the matching of field values ($|\alpha| = 0$) and higher-order derivative information. When $q = 1$, the loss corresponds to an L^1 Sobolev loss, while $q = 2$ gives a squared L^2 Sobolev loss. In practice, the derivative order depends on the PDE family. We set $p = 2$ for incompressible Navier–Stokes and diffusion–reaction systems, and $p = 1$ for compressible Euler, compressible Navier–Stokes, wave equations, and shallow-water equations.

Table 8: Sobolev derivative order p used for evaluation.

PDE Category	Sobolev Order	Poseidon Datasets	VICON Datasets	MPP Datasets
Incompressible Navier–Stokes	2	NS-PwC, NS-BB	NS2D	IncompressibleNS
Compressible Euler	1	CE-RM, CE-RPUI	Euler-2D	-
Compressible Navier–Stokes	1	-	Comp-2D	CompressibleNS
Wave Equations	1	Wave-Gaussian, Wave-Layer	-	-
Shallow Water	1	-	-	ShallowWater
Diffusion–Reaction	2	-	-	DiffusionReaction

Divergence-Free Error. For a predicted two-dimensional velocity field $\hat{\mathbf{u}} = (\hat{u}, \hat{v})$, incompressibility requires $\nabla \cdot \hat{\mathbf{u}} = 0$. We quantify the violation of this constraint by the mean absolute divergence:

$$\mathcal{L}_{\text{div}} = \frac{1}{|\Omega_h|} \sum_{\mathbf{r} \in \Omega_h} |\nabla \cdot \hat{\mathbf{u}}(\mathbf{r})| = \frac{1}{|\Omega_h|} \sum_{\mathbf{r} \in \Omega_h} \left| \frac{\partial \hat{u}}{\partial x}(\mathbf{r}) + \frac{\partial \hat{v}}{\partial y}(\mathbf{r}) \right|. \quad (35)$$

Vorticity Error. Vorticity measures local rotational dynamics of the flow. For a two-dimensional velocity field $\mathbf{u} = (u, v)$, the scalar vorticity is defined as

$$\omega = \frac{\partial v}{\partial x} - \frac{\partial u}{\partial y}. \quad (36)$$

Similarly, for the predicted velocity field $\hat{\mathbf{u}} = (\hat{u}, \hat{v})$, we compute

$$\hat{\omega} = \frac{\partial \hat{v}}{\partial x} - \frac{\partial \hat{u}}{\partial y}. \quad (37)$$

We compare the predicted and reference vorticity fields using

$$\mathcal{L}_{\text{vort}} = \frac{1}{|\Omega_h|} \sum_{\mathbf{r} \in \Omega_h} |\hat{\omega}(\mathbf{r}) - \omega(\mathbf{r})|. \quad (38)$$

This metric captures whether compression preserves fine-scale rotational structures that may not be visible from velocity error alone.

Together, these metrics evaluate not only predictive accuracy, but also smoothness, derivative fidelity, and physical consistency of compressed models.

D Trace-Based Energy Balancing for Multi-Physics Models

Unified multi-physics models such as VICON [4] and MPP [17] are calibrated on heterogeneous physical datasets whose state variables can differ greatly in numerical scale. Directly pooling all calibration samples may therefore make the clean input covariance $\Sigma_{\mathbf{X}\mathbf{X}}$ and the Fisher sensitivity matrix $\mathbf{F}_{\mathbf{Z}} = \mathbf{L}^\top \mathbf{L}$ dominated by high-energy domains. Since our greedy rank allocation ranks singular components of $\mathbf{L}_l \mathbf{W}_l \mathbf{R}_l^c$, this can bias the allocated ranks toward numerically large domains rather than loss-sensitive ones.

To mitigate this effect, Ours* applies trace-based energy balancing when estimating the calibration statistics used for rank selection. For each layer l and physical dataset $c \in \mathcal{C}$, we compute the category-specific clean covariance $\Sigma_{\mathbf{X}\mathbf{X},l}^{(c)}$ and Fisher matrix $\mathbf{F}_{\mathbf{Z},l}^{(c)}$. For the input covariance, we define

$$E_{l,c}^X = \text{Tr}(\Sigma_{\mathbf{X}\mathbf{X},l}^{(c)}), \quad \tau_l^X = \max_{c \in \mathcal{C}} E_{l,c}^X, \quad (39)$$

and rescale each domain by

$$s_{l,c}^X = \begin{cases} \tau_l^X / E_{l,c}^X, & E_{l,c}^X > \epsilon, \\ 1, & \text{otherwise,} \end{cases} \quad (40)$$

where $\epsilon = 10^{-15}$ prevents division by zero. The balanced clean covariance is then

$$\bar{\Sigma}_{\mathbf{X}\mathbf{X},l} = \frac{1}{|\mathcal{C}|} \sum_{c \in \mathcal{C}} s_{l,c}^X \Sigma_{\mathbf{X}\mathbf{X},l}^{(c)}. \quad (41)$$

The Fisher matrix is balanced analogously using its own trace:

$$\bar{\mathbf{F}}_{\mathbf{Z},l} = \frac{1}{|\mathcal{C}|} \sum_{c \in \mathcal{C}} s_{l,c}^F \mathbf{F}_{\mathbf{Z},l}^{(c)}, \quad s_{l,c}^F = \frac{\max_{c' \in \mathcal{C}} \text{Tr}(\mathbf{F}_{\mathbf{Z},l}^{(c')})}{\text{Tr}(\mathbf{F}_{\mathbf{Z},l}^{(c)})}. \quad (42)$$

We then factorize $\bar{\Sigma}_{\mathbf{X}\mathbf{X},l} = \bar{\mathbf{R}}_l^c \bar{\mathbf{R}}_l^{c\top}$ and $\bar{\mathbf{F}}_{\mathbf{Z},l} = \bar{\mathbf{L}}_l^\top \bar{\mathbf{L}}_l$, and use the singular values of

$$\bar{\mathbf{L}}_l \mathbf{W}_l \bar{\mathbf{R}}_l^c \quad (43)$$

for greedy rank allocation. Thus, the score

$$v_{l,i} = \frac{\sigma_{l,i}^2}{P^{(l)}} \quad (44)$$

is less affected by raw domain scale and better reflects loss sensitivity across the multi-physics calibration set.

In the implementation, after ranks are selected, the same trace-balancing idea can also be reused when aggregating the reconstruction statistics in Equation 6. This affects the final weight reconstruction, whereas the rank scores above depend only on the balanced clean covariance and Fisher matrices.

E Implementation Details

E.1 α : Balancing Local Approximation and Error Propagation

The hyperparameter α regulates the trade-off between preserving the intra layer reconstruction (using clean input \mathbf{X}) and maintaining output similarity under actual compression (using shifted input \mathbf{X}'),

a concept motivated by SAES-SVD [10]. Empirical evidence suggests that when input perturbations are minimal, model performance is relatively insensitive to the specific value of α . This is because the shifted activation \mathbf{X}' remains similar to the clean input \mathbf{X} , allowing our rank selection proxy—which is derived from clean activations—to remain tightly coupled with the weight reconstruction objective.

However, as the compression ratio increases and perturbations become more pronounced, prioritizing the shifted input (i.e., utilizing a larger α) becomes critical. In high-compression regimes, this focus can significantly mitigate performance collapse, for instance, reducing relative loss degradation from 3000% to 1000%. Consequently, we set $\alpha = 0.7$ as the default. This provides a robust balance that excels under aggressive compression while remaining competitive at lower compression ratios.

E.2 λ : Balancing Base Loss and Sobolev Fidelity

The magnitude of the Sobolev loss often significantly exceeds that of the model base loss, necessitating a rescaling factor λ to align their numerical ranges. Empirical investigations reveal that once magnitude alignment is achieved, further increasing the weight of the Sobolev loss—specifically to an order of magnitude higher than the base loss—yields superior compression outcomes. This observation suggests that for PFMs, prioritizing high-order structural information provides a potent form of structural regularization. By emphasizing derivative consistency, the framework effectively guides the compression process to preserve governing dynamics and physical laws, which are more sensitive to parameter perturbations than zeroth-order numerical values.

E.3 Numerical Stability and Positive Definiteness

Standard whitening techniques typically rely on Cholesky decomposition (e.g. $\Sigma_{\mathbf{c}_{\text{cov}}} = \mathbf{R}\mathbf{R}^\top$), which strictly requires the matrix to be positive definite (PD). However, when the number of calibration samples is smaller than the activation dimension (same for \mathbf{F}_z), the covariance matrix becomes rank-deficient and merely positive semi-definite (PSD), causing Cholesky decomposition to fail.

To overcome this bottleneck, we employ a robust fallback strategy inspired by the dual-SVD formulation in SVD-LLM V2 [27]. Specifically, we add a negligible diagonal perturbation (ϵI) to foster PD properties for Cholesky decomposition. If numerical instability persists, we switch to an Eigendecomposition (EVD) approach:

$$\Sigma_{\mathbf{c}_{\text{cov}}} = \mathbf{U}\mathbf{\Lambda}\mathbf{U}^\top, \tag{45}$$

where \mathbf{U} is the orthogonal eigenvector matrix and $\mathbf{\Lambda}$ is the diagonal matrix of non-negative eigenvalues. We then construct the equivalent factor $\mathbf{L} = \mathbf{U}\mathbf{\Lambda}^{1/2}$. Because EVD is mathematically equivalent to SVD for symmetric PSD matrices, this approach bypasses the strict PD requirement and perfectly preserves the theoretical minimum truncation loss, ensuring highly effective and robust compression even under extreme low-sample regimes.

F Baseline Implementation Details

F.1 ASVD

We follow the original ASVD pipeline [30] without modification to the core algorithm. For activation profiling, we use the magnitude-based scaling method with $\alpha = 0.5$. Sensitivity is estimated via the stable-rank metric, which avoids the cost of forward-pass evaluation. The candidate parameter retention ratios are $\mathcal{R} = \{0.1, 0.2, \dots, 0.9\}$. Per-layer truncation ranks are determined by binary search under a global Linear-layer parameter budget, and singular values are absorbed evenly into both factors ($\sigma_{\text{fuse}} = UV$).

F.2 Dobi-SVD

We strictly follow the default hyperparameter settings and core differentiable SVD mechanics of the original Dobi-SVD [25] framework. The only necessary adaptation is a loss scaling mechanism to address the extreme disparity in gradient magnitudes between language and physical models. LLMs optimize Cross-Entropy loss, where the exponentiated loss (Perplexity) typically hovers around ~ 20 . In contrast, PDE models like Poseidon optimize a highly normalized Mean Squared Error (MSE) that

is orders of magnitude smaller (~ 0.001). Directly applying Dobi-SVD would result in vanishing gradients for the SVD truncation parameters (γ). To bridge this gap and align the gradient spaces, we introduce an exponential loss scaling strategy: $\mathcal{L}_{scaled} = \exp(w \times \text{MSE}) - 1$, with the scaling weight w empirically set to 3000. This ensures the scaled physical loss yields gradient magnitudes comparable to those in LLMs, allowing the original optimizer logic to function effectively.

Discussion. Dobi-SVD is vulnerable to a gradient-myopia failure mode when transferred to Poseidon. Although the exponential loss scaling restores the overall gradient magnitude, it does not alter the locality of the tanh-based truncation derivative. Specifically, the soft truncation mask is defined as

$$T_i(\gamma) = \frac{1}{2} \tanh(\beta(\gamma - i)) + \frac{1}{2}, \quad (46)$$

whose derivative with respect to the truncation parameter γ is

$$\frac{\partial T_i}{\partial \gamma} = \frac{\beta}{2} \text{sech}^2(\beta(\gamma - i)). \quad (47)$$

This derivative is sharply concentrated around the current truncation boundary $i \approx \gamma$, with an effective support controlled by $1/\beta$. Consequently, a layer initialized with a truncation position far below its true rank requirement receives little or no gradient signal from the higher-rank singular components that would substantially reduce the task loss.

In our implementation, this locality is further amplified because the low-rank SVD is computed only within a small neighborhood of the current γ . That is, singular components beyond the current SVD window are absent from the computational graph, rather than merely being assigned small truncation gradients. As a result, even if increasing the rank of a sensitive layer would significantly improve the physical prediction loss, the optimizer may fail to detect this direction. Other, less sensitive layers can instead retain higher ranks to satisfy the global compression constraint, leading to a stable but suboptimal rank allocation from which the optimization cannot easily escape.

F.3 SAES-SVD

We integrated the SAES-SVD [10] framework strictly following the optimal hyperparameter settings recommended in the original paper. For the Adaptive Collaborative Error Suppression (ACES) mechanism, the authors suggest bounding the alignment strength α within $[0.25, 0.75]$ to achieve the best performance trade-off. We adopted this exact constraint. Based on the framework’s formulation $\beta = \frac{\alpha}{1+\alpha}$, this maps to a search interval of $\beta \in [0.2, 0.428]$ in our implementation.

F.4 FWSVD and SVD-LLM V2

As FWSVD [9] and SVD-LLM V2 [27] do not require explicit hyperparameter tuning, we strictly adhere to their official implementation pipelines.